A 65-nm CMOS Fluorescence Sensor for Dynamic Monitoring of Living Cells

Fatemeh Aghlmand, *Member, IEEE*, Chelsea Y. Hu, Saransh Sharma, *Member, IEEE*, Krishna Pochana, *Member, IEEE*, Richard M. Murray, *Fellow, IEEE*, and Azita Emami, *Senior Member, IEEE*

Abstract— Integrating silicon chips and live bacterial biosensors in a miniaturized "cell-silicon" system can enable a wide range of applications in smart medicine and environmental sensing. Such integrated systems need on-chip optical filtering in the wavelength range compatible with fluorescent proteins (FPs), which are the widely used signal reporters for bacterial biosensors. However, the operating range of the prior works falls short in detecting the FP signals. Here, we report a fully integrated fluorescence (FL) sensor in 65-nm standard CMOS comprising on-chip bandpass optical filters, photodiodes (PDs), and processing circuitry. The metal/dielectric layers in CMOS are employed to implement low-loss cavity-type optical filters achieving a bandpass response at 600- to 700-nm range suitable to work with FPs. The sensitivity of the sensor is further improved in the electrical domain by using a capacitive transimpedance (C-TIA) with variable switched-capacitor gain, a voltage-controlled current source (VCCS), and feedback-controlled low-leakage switches, resulting in a minimum measured current of 1.05 fA with SNR > 18 dB. The sensor can measure the dynamics of the FL signal as well as the growth of living *E. coli* bacterial cells. By employing a differential design and layout, the sensor can distinguish two biochemical signals by measuring two FPs encoded in a single bacterial strain. Using optogenetic control, a proof of concept is demonstrated to establish bidirectional communication between living cells and the CMOS chip. This integrated system creates a promising platform for the development of future closed-loop therapeutics.

Index Terms— Bacteria, bidirectional communication, biosensors, cavity, CMOS, dynamics, environmental sensing, fluorescence (FL), fluorescent protein (FP), optical filter, smart medicine, surface plasmon polariton (SPP).

I. Introduction

IN THE current era of smart healthcare, there is an increasing demand for portable, low-cost, and wearable devices that can continuously monitor, detect, and analyze biological signals for early disease diagnostics. Traditional biosensors heavily rely on biochemical reactions with a transducer that converts the chemical signal into a measurable signal in the electrical, magnetic, or optical domains [1], [2], [3], [4], [5].
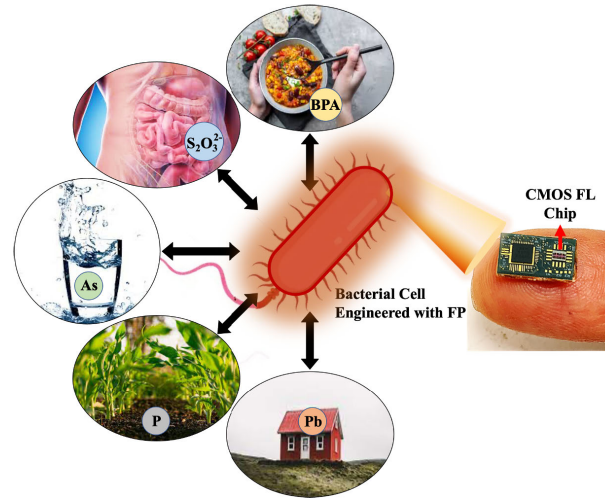
Fig. 1. Applications of a bacteria-based integrated CMOS FL sensor for detecting biochemicals in various environments.

Incorporating biochemical components within a transducer is often challenging and costly. Bacterial cells on the other hand are natural biosensors due to their ability to respond to the changes in their environment, ranging from our gut to our houses [6], [7], [8], [9], [10], [11] (Fig. 1). These cells have evolved to perceive and react to diverse chemical and physical cues, such as nutrient availability, temperature, and pH. This sensing prowess especially enables bacterial cells to detect traces of small molecules, differentiate between similar compounds, and discern subtle alterations in their surroundings. They mostly execute this task through specialized receptor proteins located on the cell surface. When these receptors interact with their corresponding ligands, they trigger a signaling cascade within the cell, leading to a cellular response [12]. Synthetic biology repurposes these cellular components by genetically engineering the bacteria to detect a wide range of analytes. Using reporter genes, the cells can produce a measurable signal in response to the presence of the target molecule, such as heavy metals [13], biotoxins [14], and inflammations.

Fluorescent and luminescent proteins are the most common choices for generating a measurable signal in the optical domain. Detecting the weak optical signal from these proteins in living bacterial cells requires bulky laboratory setups, which severely limit the application of bacteria-based biosensor

technologies in portable healthcare [15]. More recently, smaller commercial systems for mobile fluorescence (FL) detection have emerged [16]. Relying on various optical components including several front lenses, bandpass filters, dichroic mirrors, high-power LEDs, and sensitive photodiodes (PDs); the sensor in [16] covers a detection wavelength range of 460–980 nm and can support fluorescent dyes with as low as 20 nm of Stokes shift. While offering a wide operating range, the required power (1.5 W) and dimensions ($64 \times 47 \times 17.8$ mm^3) of this sensor are still far from being suitable for miniaturized portable or ingestible applications as they lack integration with the low-power and low-cost CMOS technology. Therefore, there is a pressing need for a miniaturized system that can integrate versatile sensing capabilities of live bacterial cells with the processing circuitry for real-time and reliable signal measurement and reporting.

Prior works [5], [17] demonstrated a single-chip device to detect the FL response of quantum dots (QDs) by designing on-chip high-pass optical filters. QDs are bright, durable synthetic labels mainly used in bioimaging. However, being inorganic, they are not suitable signal reporters for living cells. As the reported wavelength range of [5] and [17] is limited to the very high end of the spectrum (800 nm), these systems are not equipped to work with fluorescent proteins (FPs), which are between 400 and 700 nm [18]. In other work [19], researchers demonstrated the potential of assaying biological output signals by a single-chip sensor to detect the optical signal from luminescent proteins, which are a class of proteins emitting light without optical excitation. Hence, the system in [19] avoids the challenge of on-chip optical filtering. However, while luminescent proteins are suitable outputs for genetically modified biosensors, they are energy consuming for the host cells and would become dimmer over time. In addition, since a light source is not required to activate their light emission, the luminescence signal would interfere with the optical density (OD) detection, which is needed to monitor cell growth.

FPs are versatile and well-adopted signal reporters in synthetic biology with diverse optical profiles, allowing the detection of multiple signal outputs [20]. Developing an integrated and miniaturized cell-silicon system capable of assaying FL signals expressed by live bacterial cells opens up a new class of opportunities in medical diagnostics and environmental sensing. Another potential advantage of such a system is gene expression control via silicon chips. Encoding the genetically engineered bacterial cells with designed DNA sequences enables the production of desired enzymes, nucleic acids, and small molecules in these cells. In medicine, bacteria can be employed for delivering anticancer [21] or anti-inflammatory [22], [23], [24] compounds to treat diseases (Fig. 2). In environmental remediation, bacterial cells can produce enzymes to degrade contaminants, such as plastic [25] and oil spills [26]. However, optimizing gene expression dynamics through feedback control has been a significant challenge in synthetic biology due to the difficulty in real-time monitoring of cell dynamics [27]. Therefore, a cell-silicon system has great potential for enabling feedback control of living cell dynamics.
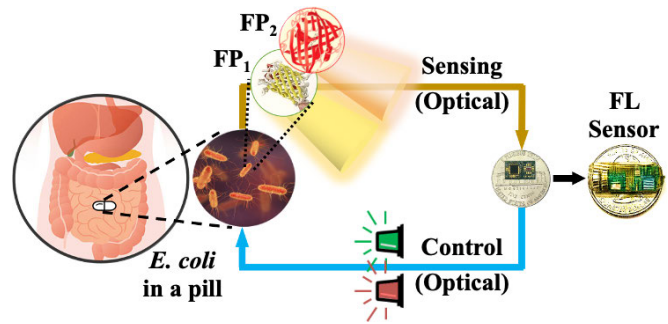

Fig. 2. Bidirectional communication system between the CMOS chip and living cells in the gut.

This article presents a miniaturized biosensing system facilitating bidirectional communication between a CMOS chip and living cells. The fully integrated FL sensor employs the metal/dielectric layers in a standard CMOS process to implement low-loss cavity-type bandpass optical filters allowing the use of engineered bacterial cells for in vivo applications. The sensitivity of the sensor is enhanced by designing bandpass PDs, and by taking advantage of a differential measurement scheme and common-mode (CM) signal rejection in the electrical domain. Furthermore, the differential design of the sensor facilitates the simultaneous measurement of two FPs with high efficiency. The functionality of bidirectional communication is validated by continuous dynamic measurement of bacterial cells which are encoded with an FP regulated by optogenetic control [28]. We demonstrate that the FP expression of cells is either enabled when they receive a green light or disabled when a red light is present.

This article, expound upon [29], is organized as follows. Section II presents the overview of the FL sensor and describes the requirements for an integrated system. Section III reviews the main resonance mechanisms for implementing optical filters and their limitations. Section IV discusses the CMOS implementation of integrated filters and PDs. The CMOS circuit design of the sensor is described in Section V, and Section VI discusses the measurement results.

II. SYSTEM OVERVIEW

A. FL Detection

FL is a category of luminescence processes in which specific molecules respond to an external excitation by emitting light after a brief interval [30]. Exciting a material with light (λ_{EX}) causes electrons in the stable states to acquire energy and transition to the higher energy bands. Due to heat and collisions with other electrons, the unstable electrons lose energy and return to their stable states. In this process, a weak light at λ_{EM} is released, indicating the presence of the desired molecules. For the concentration (C) of the fluorophores, the emitted light intensity (I_{FL}) is proportional to the excitation light intensity (I_{EX}) as follows:

$$I_{FL} = I_{EX} \cdot QY \cdot \left(1 - 10^{-\alpha Cl}\right) \tag{1}$$

where QY and $\alpha(M^{-1} \cdot cm^{-1})$ are the quantum yield and the molar extinction coefficient of the fluorophores, respectively,

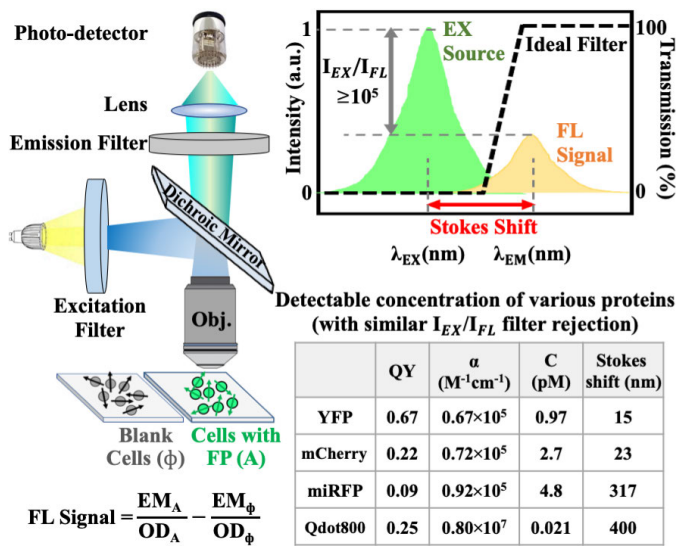This article has been accepted for inclusion in a future issue of this journal. Content is final as presented, with the exception of pagination.

AGHLMAND et al.: 65-nm CMOS FLUORESCENCE SENSOR FOR DYNAMIC MONITORING 3

$$\text{FL Signal} = \frac{EM_A}{OD_A} - \frac{EM_\phi}{OD_\phi}$$

Detectable concentration of various proteins (with similar I_{EX}/I_{FL} filter rejection)

	QY	α ($M^{-1}cm^{-1}$)	C (pM)	Stokes shift (nm)
YFP	0.67	0.67×10^5	0.97	15
mCherry	0.22	0.72×10^5	2.7	23
miRFP	0.09	0.92×10^5	4.8	317
Qdot800	0.25	0.80×10^7	0.021	400

Fig. 3. Traditional FL sensor and relative intensity levels of the excitation source and FL signal.

Fig. 4. Conceptual overview of the integrated FL sensor.

and l(cm) is the optical path length. Even though (1) suggests a stronger excitation light results in a higher emission signal, such illumination may cause photobleaching of the fluorophores, resulting in severely limiting or even terminating their ability to fluoresce [31].

While the level of the EX source is kept at a safe limit, the strength of the emitted FL light is determined by C and the characteristics (QY, α) of the selected protein. Most of the common FPs that are used extensively with live bacterial cells provide an α of lower than 1×10^5, lie in the lower range of the visible spectrum, and have a small Stokes shift ($\approx$15–30 nm). This implies that the sensor not only must be highly sensitive to the weak FL signal but also should provide a large rejection of EX light, which is very close to the EM band. For instance, based on (1), a 10-pM concentration of yellow fluorescent protein (YFP) results in a ratio of 10^{-6} for the FL emitted light (at 530 nm) to the EX light (515 nm) for a path length of 1 cm. This shows the importance of a high-rejection ratio needed for FL detection, which is more than 60 dB for most traditional sensing systems that use several optical components.

Fig. 3 shows that traditionally measuring the FL signal of a protein involves using two cultures. The control culture (ϕ) contains blank bacterial cells to account for their auto-FL response, and the primary culture (A) includes bacterial cells engineered with the desired FP. The FL signal is then calculated by subtracting the emission of culture ϕ from the emission of culture A after being normalized to their respective OD, which is a measure of the cell population. To measure OD, light at a specific wavelength (usually 600 nm) is transmitted through the sample of cells and subsequently collected by a photodetector. As cells grow, more light is absorbed and scattered, resulting in less light reaching the detector [32]. In this work, the goal is to provide both FL and OD measurements.

B. Integrated FL Sensor

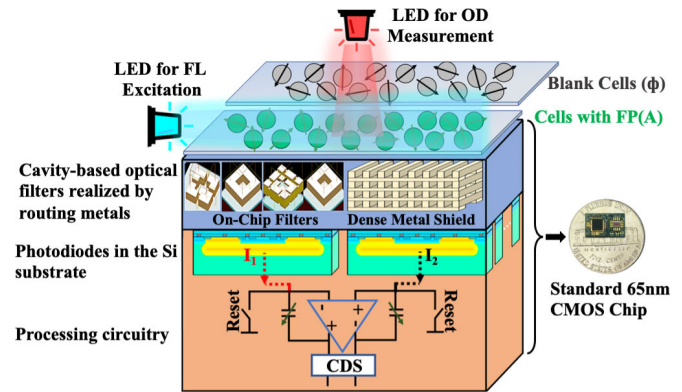As discussed, the most critical challenge in realizing the fully integrated FL sensor is implementing narrowband optical filters to reject the strong excitation light close (in wavelength) to the weak emission signal. Implementing spectral filters which are efficient, scalable, and low cost has been the subject of active research, particularly for image sensors. Due to shrinking pixel size, conventional dye-based filters fabricated by superimposing a dye-doped polymer on each pixel show severe limitations [33]. Other than the required carefully aligned lithography steps which make their scalability an issue, the crosstalk of these filters could be quite high due to the large vertical distance between the filter (on top of the sensor) and the PD (in the silicon substrate) [34]. These issues can be greatly reduced when spectral filtering is achieved through interaction between light and nanostructures, as opposed to the absorptivity of a material (i.e., dyes). These inherently compact designs can be implemented in arbitrary geometries and by using low-loss metal or all-dielectric materials, located close to the PD for achieving lower crosstalk [35], [36], [37], [38].

CMOS process offers a cost-effective platform for integrating optical/electrical components of a system in a single chip. Thanks to the accessible sub-wavelength feature size and availability of multiple metal and dielectric layers, nanostructures can be designed in CMOS to realize optical filters. Furthermore, the PD implemented in the silicon substrate directly converts the light to an electrical signal, which is then efficiently processed on the same chip. Therefore, using a standard CMOS process without additional fabrication steps to integrate the FL sensor results in a low-cost and miniaturized sensor suitable for portable applications (Fig. 4). Nonetheless, standard CMOS technology poses several challenges in implementing efficient optical filters. In addition to the fixed material of the stack-up, there is no comprehensive information about all the layers. Strict design rule checks (DRCs) of CMOS limit geometries with certain shapes and dimensions and enforce the use of lossy metal layers. Hence, understanding the behavior of metals at optical frequencies is imperative.

Optical properties of metals vary significantly over a wide frequency range, from being highly reflective in the microwave and far-infrared range up to a near-dielectric behavior in the UV range. At higher frequencies, field penetration into metal increases resulting in more dissipation and attenuation. Using the complex dielectric function $\varepsilon(\omega)$, these various dispersive
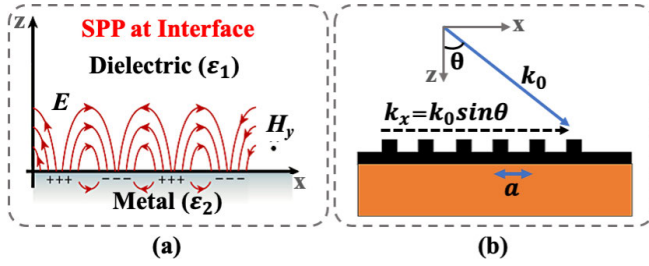
Fig. 5. Characteristics and excitation of SPP. (a) Composed character of SPP at the interface between dielectric and metal. (b) One-dimensional periodic grating as the common method to excite SPP.
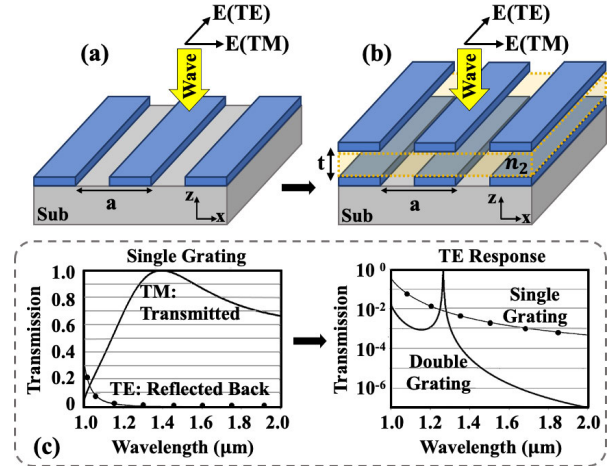

Fig. 6. Comparison between TM and TE responses of single and double gratings. (a) Single grating structure supports SPP. (b) Double grating structure supports guided mode. (c) TM and TE responses of two structures.

properties of metals can be studied [39]. Specifically, comparing $\varepsilon_{im}(\omega)$ of copper (Cu) which is the available metal in CMOS, with gold (as the standard metal) reveals a distinctly higher attenuation of Cu when exposed to the optical signals at a wavelength range lower than 600 nm [5]. This observation helps in deciding the best type of dominant resonance mechanism for the bandpass optical filter in terms of loss. In addition, the selected resonance type should have low sensitivity to the angle of arrival (AOA) of the incoming light and its polarization since cells in a biological culture are considered unpolarized light dipoles emitting in random directions/polarizations.

III. Optical Filter Design

The study of electromagnetic wave interaction with metal/dielectric interfaces has steadily gained interest in recent years [40], [41], [42]. Various optical functions can be implemented by manipulating the electric field through metallic nanostructures. A wide range of applications includes the development of nanoantennas/arrays for biological and chemical sensors [43], [44], sub-wavelength waveguides [45], solar cells [46], and narrowband optical filters [47], [48], [49]. Three main categories of optical resonances that can be used in implementing the filters are discussed as follows.

A. Surface Plasmon Polariton

When an electromagnetic wave interacts with a metal/dielectric interface, under boundary conditions satisfied only in the TM polarization, a propagative surface wave can exist along the interface, called surface plasmon polariton (SPP) [36]. Solving the Maxwell equations in the metal and dielectric parts of the interface results in the following equation, describing a wave propagating along the x-direction with the electric field E as

$$E(x, y, z) = E(z)e^{i\beta x} \quad \text{and} \quad \beta = k_0\sqrt{\frac{\varepsilon_1\varepsilon_2}{\varepsilon_1 + \varepsilon_2}} \quad (2)$$

where $E(z)$ is the normal component of the E-field, β is the propagation constant of traveling waves in the x-direction, ε_1 and ε_2 are the dielectric constants of dielectric and metal mediums, and k_0 is the wave vector of free space light. SPP is composed of an EM wave in the dielectric medium and an oscillating electron plasma in the metal [Fig. 5(a)], where both modes have exponentially decaying evanescent characteristics. Due to the lower dispersion relation of SPP than light at all non-zero frequencies, this resonance cannot

be excited by direct light illumination as energy, and momentum conservation cannot be simultaneously satisfied, and a momentum transfer is needed [50]. Grating structures with the period (a) and described by the grating equation in the following equation are one of the most common ways of satisfying this momentum mismatch [48]

$$\beta = k_0 \cdot \sin\theta \pm 2\pi n/a, \quad n = 1, 2, \ldots \quad (3)$$

where θ is the angle of the incident as shown in Fig. 5. Even though the SPP resonance can be very sharp, the strong dependency between its resonance wavelength and θ makes it unsuitable for the FL sensor with the random incident angle. In addition, the metallic loss is a major concern for SPP since part of this wave needs to propagate inside the metal, making it less attractive in CMOS with copper as the available metal and due to strict DRC enforcing minimum metal area usage.

B. Guided-Mode Resonance

It is instructive to consider the single grating structure in TE polarization, where SPP cannot exist. As shown in Fig. 6(c), while the TM transmission of this structure is relatively high (due to SPP), the TE wave is mainly reflected. Adding the second row of the identical grating on top introduces constructive interferences of transmitted and reflected light by two consecutive structures. As a result, at some optogeometrical parameters, the double grating structure can achieve high transmission and support guided mode in TE polarization [52]. For the double grating structure [Fig. 6(b)], surrounded by a medium with refractive index n_2 and infinite in the y-direction, the following holds [53]

$$n_2^2 k_0^2 = k_x^2 + k_y^2 + k_z^2, \quad k_y = 0 \quad (4)$$

where k_x, k_y, and k_z are the components of the wave vector in the x-, y-, and z-directions. The grating structure shifts k_x to be $k_0\sin\theta + (2\pi n/a)$, and at the same time, the transverse resonance condition to support the guided mode in medium n_2 roughly requires $k_z = (\pi m/t)$, where t is the middle layer thickness [54]. For the normal incident ($\theta = 0$), by replacing
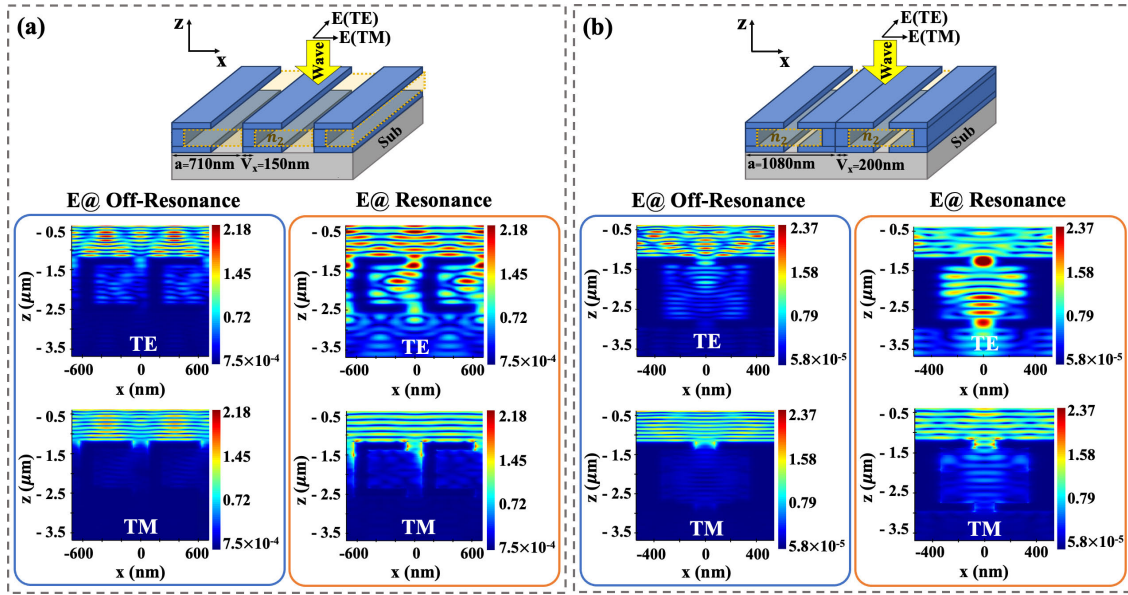
This article has been accepted for inclusion in a future issue of this journal. Content is final as presented, with the exception of pagination.

AGHLMAND et al.: 65-nm CMOS FLUORESCENCE SENSOR FOR DYNAMIC MONITORING   5

Fig. 7. Simulated E-field in TE/TM polarization for (a) One-sided 1-D cavity structure between M_7 and M_4 and (b) double-sided 1-D cavity structure between M_7 and M_3.

these components of the wave vector with their equivalent values, we get the following:

$$\left(\frac{2\pi n_2}{\lambda}\right)^2 = \left(\frac{2\pi n}{a}\right)^2 + \left(\frac{\pi m}{t}\right)^2, \quad n, m = \text{integer} \quad (5)$$

which shows that the mth mode of the slab can be excited through the nth order of grating. Solving (5) using $n = m = 1$ gives the thickness (t) for the presence of the guided mode through first-order of gratings [52]. Since the wave propagates in the dielectric area surrounded by the metal and is not coupled to the interface, this resonance is less lossy than the SPP.

In this structure, a narrow spectral response can be achieved by closing the resonator (i.e., decreasing the aperture) as it reduces the coupling with the incident light [55]. While this is desired for implementing sharp bandpass filters, exciting the waveguide mode through the first diffraction order of gratings links the incident angle θ to the wave propagation constant and hence λ. Therefore, the narrow spectrum in the wavelength results in a narrow response to θ which is not desirable due to the lack of collimated incident light in FL sensing.

C. Cavity-Mode Resonance

The mentioned challenge in the linked $\lambda - \theta$ responses of the previous two resonances can be suppressed using cavity resonances [52]. Fig. 7 shows the double grating structure with vertical metallic walls added between adjacent cells. The main function of the walls is to isolate the field inside each cell, suppressing the guided-mode resonance and supporting the cavity resonance. Choosing a large enough lateral distance between adjacent cells minimizes the overlap of the effective transmission cross section of cavities [55], [56]. This results in less coupling between the resonant cells and avoids propagative wave hopping from one cavity to another; hence, the angle dependency due to the guided mode is reduced. Similar to
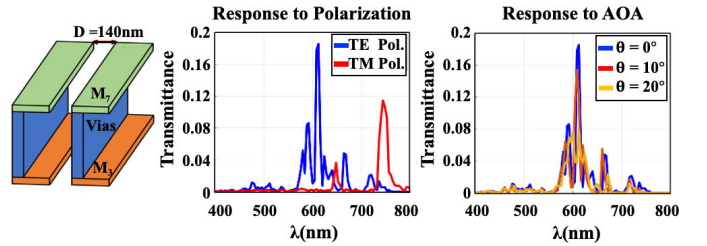

Fig. 8. One-dimensional cavity implemented in CMOS and its response to the variation of polarization and AOA.
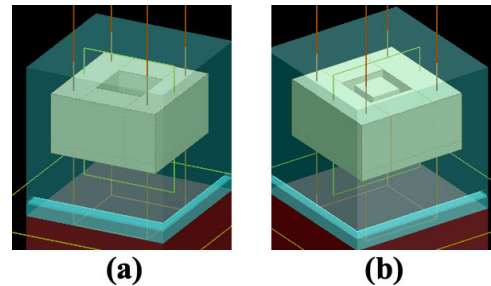

Fig. 9. Two variations of symmetric cavities for polarization-insensitive filter. (a) Two-dimensional hollow cavity. (b) Two-dimensional coaxial cavity.

the waveguide structure, closing the cavity by decreasing the aperture size reduces the spectral bandwidth; however, the response of the cavity can be narrowband in λ and broader in θ. This is achieved since this resonance mainly depends on the optogeometrical properties of the cavity, and the incident angle plays a minor role. The main effect of the incident angle variation is the change in the strength of the resonance and not the resonance wavelength.

IV. CMOS OPTICS-ELECTRONICS INTEGRATION

A. Bandpass Integrated Optical Filters in CMOS

Two variations of the 1-D cavity resonators implemented between M_7 and M_3, and M_7 and M_4 and using dense
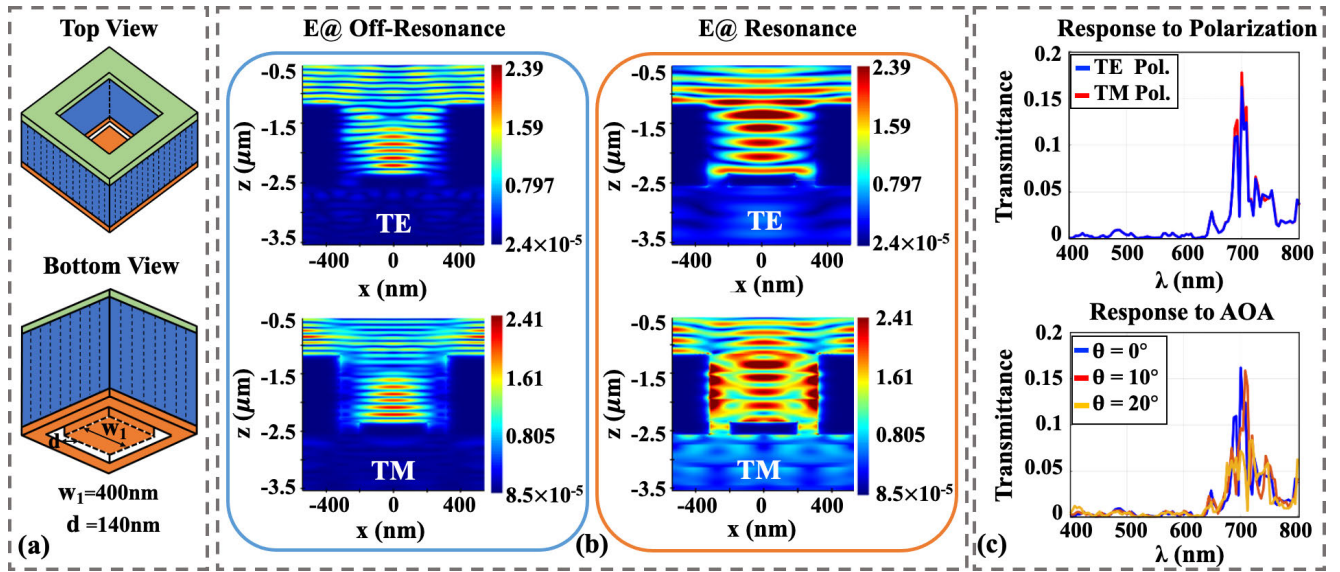
Fig. 10. Proposed 2-D cavity implemented in CMOS and its simulated results. (a) Cavity structure. (b) Simulated E-field in TE/TM polarization. (c) Response of the filter to the variation of polarization and AOA.

via arrays as vertical walls are shown in Fig. 7. Extensive finite-difference time-domain (FDTD) simulations considering all known dielectric layers in CMOS stack-up have been performed to achieve optimized structures. As the electric field patterns show, while for the TE polarization, there is a strong field enclosed by the cavity, the wave in the TM polarization is coupled to the interface and can hardly propagate up to half of the structure. The response of the one-sided cavity to the polarization and AOA variation is shown in Fig. 8. As expected, the primary transmission peak located at lower wavelengths is due to cavity mode at TE polarization, and TM response happens at higher wavelengths where the loss of copper is lower. Furthermore, we observe that variation of the incident angle primarily results in the variation of the resonance peak rather than its wavelength.

B. Polarization-Insensitive Filters

To achieve polarization-insensitive filters, geometrically symmetric structures are required. Converting the 1-D cavity to a fully symmetric structure results in the 2-D hollow square design shown in Fig. 9(a). Due to the minimum enclosed area rule by DRC, the central hollow area of the cavity is forcibly large, causing this structure to be very wideband in the wavelength of interest. Alternatively, the 2-D coaxial design [57] supporting the cavity mode in the coaxial aperture is considered next [Fig. 9(b)]. Satisfying the minimum metal area rule (in the center) and minimum enclosed area (the coaxial part) makes this cavity to be highly lossy. It is worth mentioning that for the symmetric geometries, the resonance only happens at a wavelength in which both TE and TM polarizations can propagate; therefore, the loss associated with TM transmission must be lowered. To reduce the loss of the cavity while keeping the response narrowband and satisfying the DRC rules, the solution is to minimize metal usage of the coaxial cavity. Since the large lateral distance between cavities is still required for low-angle dependency, the use of central
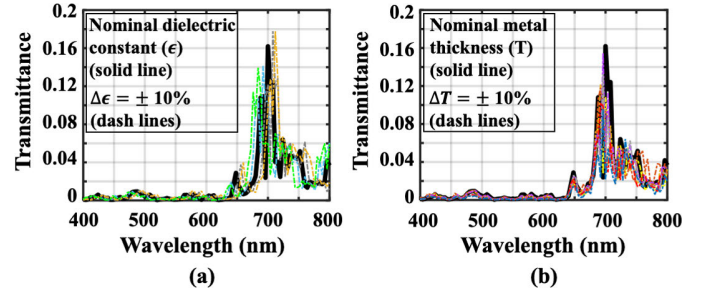

Fig. 11. Simulated performance of the 2-D filter against process variations in (a) dielectric constant of all known layers and (b) thickness of all used metal layers.

metal can be reduced. The minimum area of this metal in the XY plane still causes high loss for a cavity implemented between M_7 and M_3 layers; therefore, the metal usage in the Z-direction needs to be lowered. By keeping the central metal just in the lowest layer (M_3), the cavity of Fig. 10(a) is obtained. As the simulated electric field patterns show, at TE polarization, a cavity mode exists in the coaxial gap, and in TM polarization, the field is coupled to the external metal interface. The simulated response of this cavity to the variation of the polarization and AOA is shown in Fig. 10(c), confirming its polarization-insensitive response and tolerance to 20° of AOA variation without creating new resonance peaks.

The filter performance is also simulated with the process variation effects in the metal thickness and the dielectric constant (in all known dielectric layers). As shown in Fig. 11, for both parameters, based on the provided information in the PDK, a variation of ±10% is considered. It is observed that the dielectric constant variation mainly affects the peak wavelength of the filter, while the metal thickness variation mostly changes the intensity of the filter's peak transmission. In analyzing the effect of these variations, it is important to note that although the emission of FPs is maximum at one wavelength (λ_{EM}), as Fig. 3 shows; their emission band spans

This article has been accepted for inclusion in a future issue of this journal. Content is final as presented, with the exception of pagination.

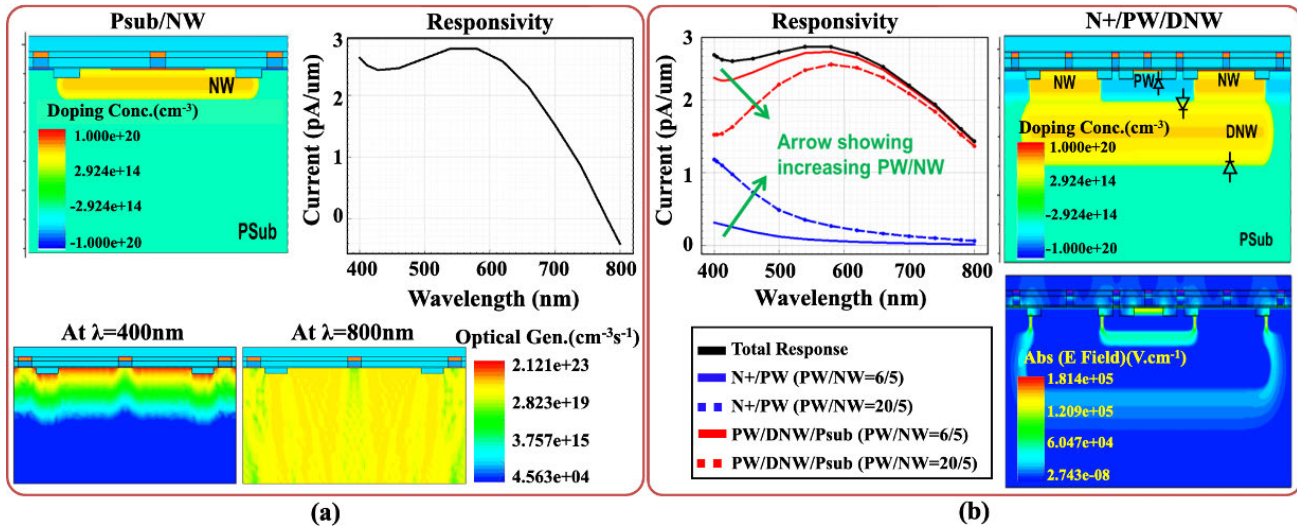AGHLMAND et al.: 65-nm CMOS FLUORESCENCE SENSOR FOR DYNAMIC MONITORING 7

Fig. 12. Design and simulation results of PDs in CMOS. (a) Psub/NW PD design, responsivity, and optical generation. (b) N+/PW/DNW PD design, responsivity, and E-field.

wider. Hence, even if due to the process variation, λ_{EM} falls out of the filter passband, the sensor is still able to capture part of the FP's emission, though with a smaller intensity. As explained later, the front end of the sensor is designed with a large dynamic range, high sensitivity, and configurability to account for the variation in the desired signal level.

C. Integrated PD in CMOS

The PD design in the standard 65-nm CMOS process is discussed in this section. To model the PD's response using TCAD Synopsis tools, the doping profile and thickness of various layers are needed, which are approximated based on the plots in [58], [59], [60], and [61]. First, the NW/Psub PD, one of the most popular choices in CMOS, is designed and simulated in 2-D using a small unit size of 10 μm [Fig. 12(a)]. Assuming that each absorbed photon can excite an electron/hole pair, the optical behavior of PD in silicon can be simulated using the generation rate G. Defined as the number of electrons excited per unit volume and per unit time, G is derived from the absorbed power in the active region and is plotted for short and long wavelengths of the incident light in Fig. 12(a). Due to the wavelength-dependent absorption length of silicon, the density of the generated electron/hole pair at 400 nm is maximum at areas close to the surface of the substrate while for the longer wavelengths, the photons need to travel more deep in the substrate to be absorbed and generate carriers.

This observation led to the design of a triple junction vertical PD of N+/P-well (PW)/deep N-well (DNW), as shown in Fig. 12(b). Although for the same unit size, the total responsivity of this diode is similar to the NW/Psub, by creating shallow and deep junctions we can achieve a bandpass response for the PD which helps in providing another level of optical filtering. The shallow junction made of the n+ layer on top of the PW is used to collect and discard the short wavelength light, and the two deeper junctions of PW/DNW and DNW/Psub convert the mid and high wavelengths of

the incident light to an electrical current. As expected, and shown by the arrow in the plot, increasing the ratio of the PW area to the NW area in a fixed DNW dimension results in a more passband response at the cost of reducing the mid-band responsivity. In simulating both PDs, the width and the number of metal contacts are kept minimum to avoid blocking the effective active area of the diodes. Furthermore, since the main process contributing to the PD current in the low-speed operation is diffusion rather than drift, the size of the depletion region where the majority of the dark current is generated is optimized for achieving lower dark current at the cost of slightly lower responsivity.

V. INTEGRATED CMOS CIRCUIT DESIGN

The architecture of the CMOS FL sensor is shown in Fig. 13. It contains six rows of front-end circuitry to process the signal of various optical filters and PDs which are placed differentially between the center and right/left columns of the chip. In each row, a capacitive transimpedance amplifier (C-TIA) with a variable capacitor bank in the feedback is used to convert the differential PD current to voltage. A correlated double sampler (CDS) block samples the buffered output of the C-TIA twice to remove the offset and the low-frequency correlated noise components [62]. To save area and reduce power consumption, one CDS block is shared for every four rows using CDS-Sel switches. In addition, a resistive adder block is designed to combine the response of several rows of the chip to gain a stronger signal, if desired. By doing so, a uniform size of PD pixel is kept throughout the chip and the configurability of the design is increased by combining the signals in the voltage domain, thus avoiding extra routing in the PD active area. The sensor also includes an on-chip temperature sensor, a clock generator, and a digital scan chain block to distribute all the digital control bits of the circuit.

The timingdiagram of the circuit is shown in Fig. 13. During phase 1, the C-TIA integrates the PD current on the feedback capacitor bank resulting in a sawtooth voltage (VTIA), while the CDS circuit is in reset mode.

Fig. 13. Architecture of the CMOS FL sensor circuitry, showing three rows of C-TIAs, CDS, and adder blocks along with the circuit timing diagram.

Next, during phase 2, C-TIA is in reset mode, while the CDS output is ready to use. The CDS takes the first sample at the end of phase 1 (t_{s1}), storing the peak value of the VTIA$_+$/VTIA$_-$ (V_{P1}, V_{P2}) on C_1 capacitors and the second sample at the beginning of phase 2 (t_{s2}) to capture the lower value of the VTIA$_{+/-}$ waveforms (V_{B1}, V_{B2}). Writing the charge conservation equations at these two sampling times at the input nodes of the OTA$_1$, we get the following:

$$Q_{IN+}(t_{s1}) = Q_{IN+}(t_{s2}) \tag{6}$$
$$C_1(V_{CDS} - V_{P1}) + C_2(V_{CDS} - V_R) + C_f(V_{CDS} - V_{OUT-})$$
$$= C_1(V_{IN+} - V_{B1}) + C_2(V_{IN+} - V_{OUT-}) \tag{7}$$

and

$$Q_{IN-}(t_{s1}) = Q_{IN-}(t_{s2}) \tag{8}$$
$$C_1(V_{CDS} - V_{P2}) + C_2(V_{CDS} - V_R) + C_f(V_{CDS} - V_{OUT+})$$
$$= C_1(V_{IN-} - V_{B2}) + C_2(V_{IN-} - V_{OUT+}) \tag{9}$$

where Q_{IN+} and Q_{IN-} are the charges stored at the OTA$_1$'s input nodes. Defining the differential amplitude of VTIA as $V_{Diff} = [(V_{P1} - V_{B1}) - (V_{P2} - V_{B2})]$ and substituting $(V_{IN+} - V_{IN-}) = (V_{OUT+} - V_{OUT-})/A_1$ and $C_1 = C_2 = C$, we get

$$V_{Diff} = \left[1 + \frac{2}{A_1} - \frac{C_f}{C}\right](V_{OUT+} - V_{OUT-})$$
$$\approx (V_{OUT+} - V_{OUT-}). \tag{10}$$

Even though the small C_f in the feedback path is used mainly to avoid the open-loop configuration of OTA$_1$ at any time, the C_f/C can be chosen to remove the error associated with the finite open-loop gain of the OTA$_1$ (i.e., $2/A_1$).

The detailed circuit diagram of each row of the sensor is shown in Fig. 14. In a multi-pixel receiver, it is desirable to share the front-end circuitry between several PD units. In applications such as FL sensing, where the signal of interest is an extremely small current, the use of switches at the input is problematic since the CMOS transistor in its OFF state has a leakage current that can be larger than the desired input. This leakage is significantly suppressed if the off voltage across the switch is kept close to 0. As shown in Fig. 14, this is achieved by placing the switch in closed-loop feedback. Even though using these switches, the number of pixels sharing the C-TIA can be larger; in this work, we conservatively used one C-TIA per each row of the sensor. In addition, by using a complementary switching scheme, the leakage cancellation loop is efficiently shared between four switches at each input node of the C-TIA. If any of the switches are OFF, their complementary control signal is active, which places the respective switch in the controlled loop.

Facing the limitations of the standard CMOS process in realizing sharp bandpass optical filters, the circuit and footprint of the sensor are designed to boost its optical rejection while achieving high sensitivity to the weak FL signal. As shown in Fig. 3, FL detection is fundamentally a differential operation between blank cells (ϕ) and engineered cells (A). This enables us to design the sensor in such a way that it converts any unfiltered excitation light to a CM component. Therefore, by electrically rejecting this CM signal in a differential front end, the total rejection ratio of the sensor is drastically improved compared with relying solely on optical filtering. The sensor has the added advantage of combining the two measurements of cultures A and ϕ that are required for

This article has been accepted for inclusion in a future issue of this journal. Content is final as presented, with the exception of pagination.

AGHLMAND et al.: 65-nm CMOS FLUORESCENCE SENSOR FOR DYNAMIC MONITORING 9
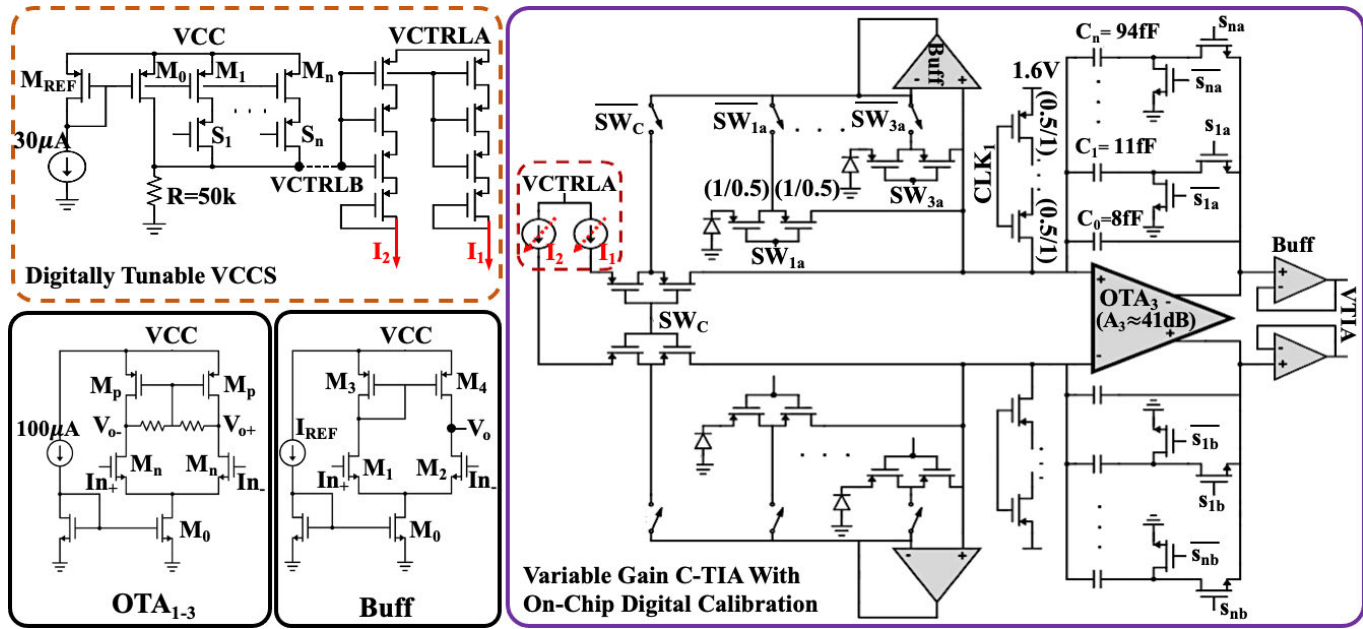

Fig. 14. Detailed circuit diagram of the variable-gain C-TIA with low-leakage switches, digitally tuned VCCS, and amplifiers.

FL detection in one, as opposed to two separate absolute measurements.

The undesired CM signal can be comprised of the dark current of the PDs, the remaining leakage of the switches, and more importantly, part of the excitation light that reaches the PD after imperfect optical filtering. To increase the front-end's ability to reject large CM signals a compensating scheme is required, especially if the feedback capacitor is kept small to achieve a high gain. A tunable voltage-controlled current source (VCCS) is designed and connected to the C-TIA using SW_C switches to provide configurability and extend the circuit's range of CM rejection. The tuning of the VCCS is done by one external course tune (VCTRLA) and one on-chip fine tune (VCTRLB) controlled via seven digital bits. Based on the simulation results, this block can compensate for up to 130 pA of CM current. Although complete CM removal seems challenging due to manual tuning, simulation results show that even with rough removal of the large CM current, the sensitivity of the circuit is drastically improved, thus eliminating the need for complete current subtraction.

To apply the required FL normalization to the respective OD of each culture in the closed-loop operation, the C-TIA is designed with individually controlled switched capacitor banks to provide independent variable gain for each feedback path. Using switches s_{na} and s_{nb}, each capacitor is either placed in the feedback path to contribute to the gain or is in the reset mode connected to the ground. Finally, the output of C-TIA is buffered to interface with the CDS and adder.

The transient simulation results of the C-TIA, CDS, and adder blocks for differential currents of 5–15 fA on top of a moderate CM current (200 fA) are shown in Fig. 15. The adder linearly combines the response of three rows (TIA1–TIA3) each with a different signal level to achieve a stronger signal. Fig. 16. shows the simulation results of the C-TIA and the
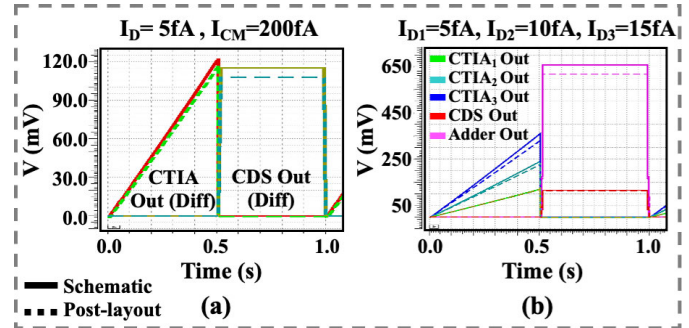

Fig. 15. Transient simulation results of (a) one row of C-TIA and CDS for $I_D = 5$ fA and (b) three rows of C-TIA and their collective signal using the adder.

effects of the variable switched-capacitor bank and VCCS block when a large CM current is present. As shown, when the LSB capacitor is used, the circuit remains almost linear for the small differential current of $I_D = 5$ fA even for a large CM current of $I_{CM} = 1$ pA. On the other hand, for a higher differential current ($I_D = 50$ fA), the circuit starts to saturate for moderate I_{CM} values. While using a most significant bit (MSB) capacitor can mitigate this problem by reducing the gain [Fig. 16(b)], the VCCS gives us another degree of freedom in extending the dynamic range of the sensor. As shown in Fig. 16(c), when a CM current of $I_{CM} = 900$ fA is present, the circuit is not completely linear even for a small I_D. Using the VCCS to partially compensate for this I_{CM} current, the circuit can provide high gain while staying linear for larger I_D currents [Fig. 16(d)]. The effect of the CDS block in reducing the offset of the sensor is shown using Monte-Carlo simulations in Fig. 17. While the peak output of C-TIA has a standard deviation of >100 mV, the CDS block samples the peak amplitude of the C-TIA and achieves a standard deviation of <7 mV.
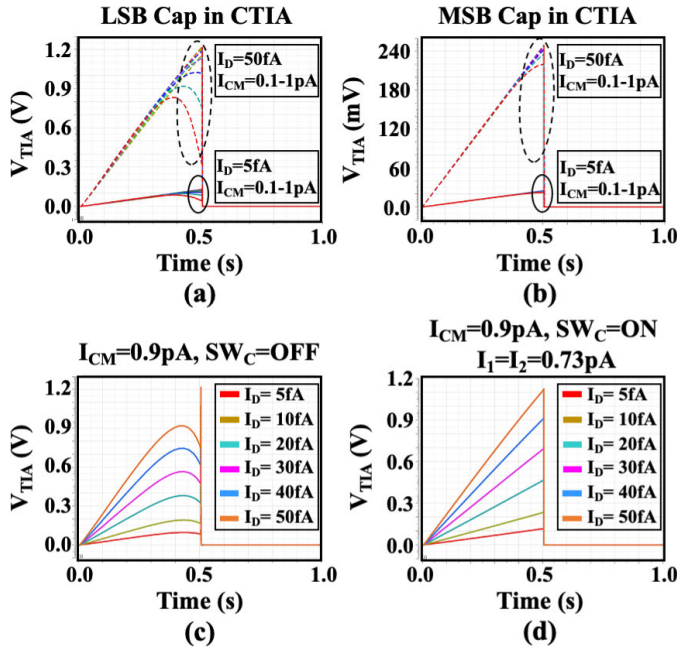
Fig. 16.   C-TIA differential output with (a) LSB capacitor in the feedback path, (b) MSB capacitor in the feedback path, (c) large I_{CM}, without compensation, and (d) large I_{CM}, with partial compensation.
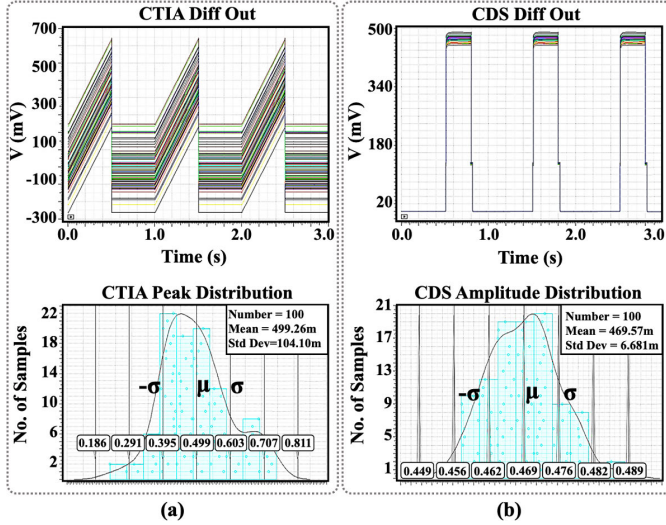

Fig. 17.   Results of Monte-Carlo simulations showing the effect of CDS in reducing the offset. (a) Variation of the C-TIA output waveform and its peak value distribution. (b) Output waveform of CDS with lower variations.

When evaluating the design tradeoffs of the FL sensor, several noise sources need to be considered. For the C-TIA, the OTA$_3$ contributes most of the thermal noise while its flicker noise is largely suppressed thanks to the CDS circuit. The input-referred current noise of the OTA$_3$ is written as follows:

$$\overline{I_{n_{in,OTA3}}^2} = \frac{4kT\gamma}{g_{mn3}}\left(1 + \frac{g_{mp3}}{g_{mn3}}\right) \cdot \omega^2(C_{GS3} + C_{FB3}(1 + A_3))^2 \tag{11}$$

$$\overline{I_{n_{in,OTA3}}^2} \approx 4kT\gamma\left(g_{mn3} + g_{mp3}\right) \cdot (\omega C_{FB3}R_{out3})^2 \tag{12}$$

where g_{mn3} and g_{mp3} are the transconductances of the input pair and load transistors, R_{out3} is the OTA$_3$'s output impedance

and C_{FB3} includes C_{GD} of the input transistors and the effective capacitor from the C-TIA's switched-capacitor bank. The switches at the front end and the PDs add shot noise to the circuit with a spectral density of $2q(I_L + I_{Dark})$, where I_L is dominated by the leakage current of the reset switches (controlled by CLK$_1$) during the C-TIA integration phase, and I_{Dark} is the dark current of the PDs. In addition to the circuit noise, the sensor suffers from photon shot noise with a spectral density of $2q(P_{FL} + (P_{EX}/\gamma))R_F$, which is mostly due to the leakage of the excitation light after imperfect filtering. Here, γ denotes the filtering ratio, and R_F is the responsivity of the PD. Considering these noise sources, (13) defines the signal-to-noise ratio (SNR) at the sensor input, where T_{int} is the integration time

$$\text{SNR} \approx \frac{P_F R_F}{\sqrt{I_{n_{in,OTA}}^2 + q(I_L + I_D)/T_{int} + q\left(P_{FL} + \frac{P_{EX}}{\gamma}\right)R_F/T_{int}}}. \tag{13}$$

Comparing the noise of these components for typical integration times of 1 s, it is seen that the most dominant noise source during the FL measurement is the photon shot noise, resulting in the simplified form as follows:

$$\text{SNR} \approx I_{in}\sqrt{\frac{T_{int}}{q(I_{in} + I_l)}} \tag{14}$$

in which $I_{in} = P_{FL}R_F$ and $I_l = P_{EX}R_F/\gamma$. As shown in (14), with the fixed γ, the SNR can be improved by increasing T_{int}. A very long integration time can cause saturation of the front-end by the PDs CM current, which is avoided here by using the tunable VCCS and switched-capacitor bank in the C-TIA. On the biology side, however, there is a limit on the maximum value of T_{int} due to the possible photobleaching of the proteins.

A detailed overview of the proposed sensor is shown in Fig. 18(a). Since any control loop requires measuring at least two substances, the reference and the target, the sensor needs to be able to detect two FPs simultaneously. This is achieved by the floor planning of the chip as shown in Fig. 18, such that it covers three wells. The center well (W1) contains the blank bacterial cells to provide a reference for the differential FL measurements of the right/left wells, making any residual excitation light to appear as a CM signal. As the zoomed-in view of each row in Fig. 18(b) shows, underneath each well there is a column for the absolute OD measurement and two PD variations for each filter type.

VI. MEASUREMENT RESULTS

The FL sensor is fabricated in a standard 65-nm CMOS process, and its die micrograph and power breakdown chart are shown in Fig. 19. The measurements have been done in optical, electrical, and biological domains. An unpolarized tunable light source with 6-nm bandwidth and a tunable neutral density filter is used for optical/electrical characterizations.

The electrical measurement results of the sensor are shown in Fig. 20. The responsivity of the bare PD1 at 700 nm is measured to be 24 mA/W. Using an integration time of 1 s,

This article has been accepted for inclusion in a future issue of this journal. Content is final as presented, with the exception of pagination.

AGHLMAND et al.: 65-nm CMOS FLUORESCENCE SENSOR FOR DYNAMIC MONITORING
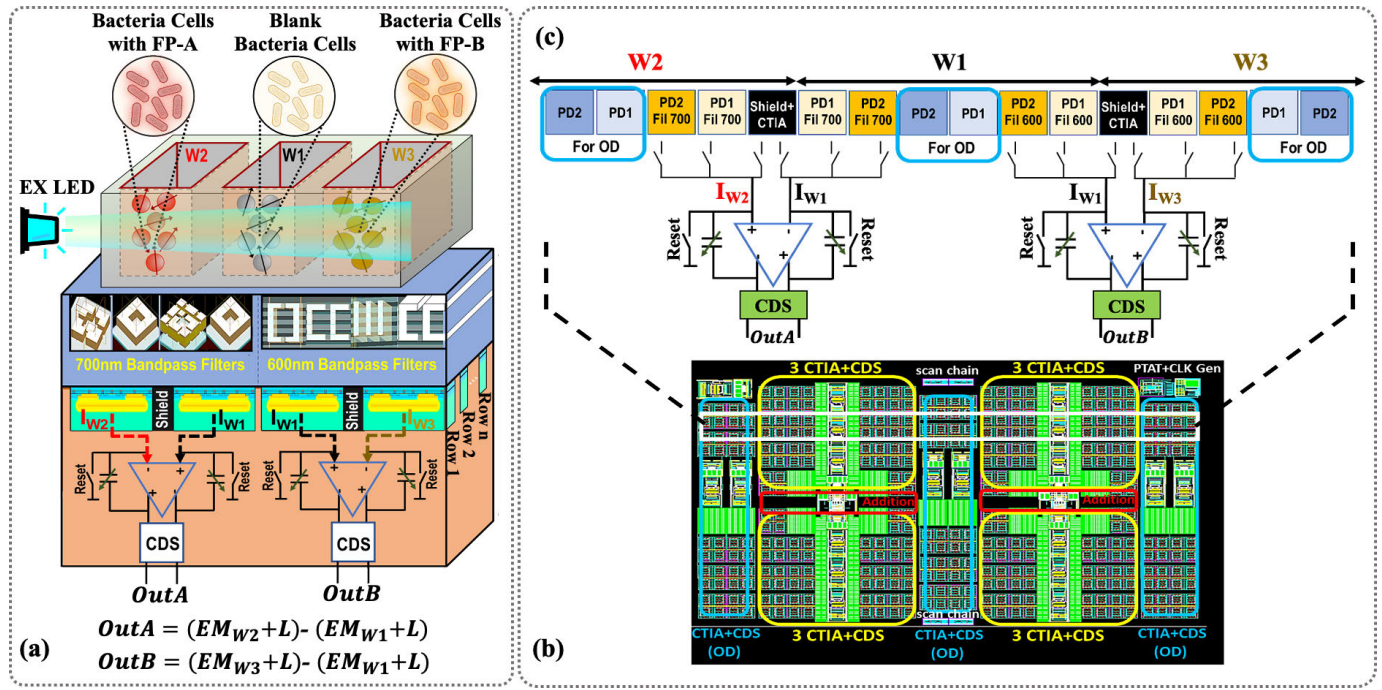
11

Fig. 18.   Overview of the sensor footprint and layout. (a) Detailed overview of the proposed differential FL sensor including the CMOS chip and the MF chamber aligned on top. (b) Layout of the chip. (c) Zoomed-in view of one row of the sensor.
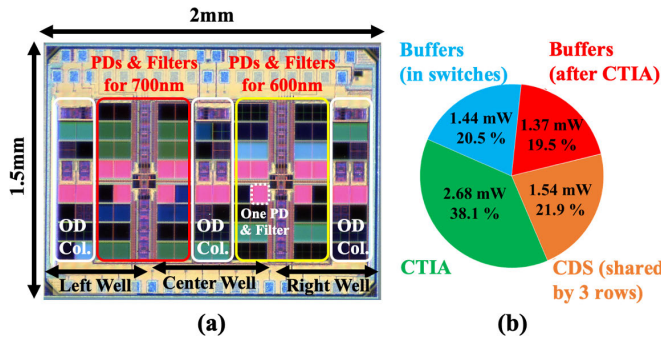

Fig. 19.   Fabricated chip and its power consumption. (a) 65-nm CMOS chip micrograph. (b) Power breakdown chart of the sensor.
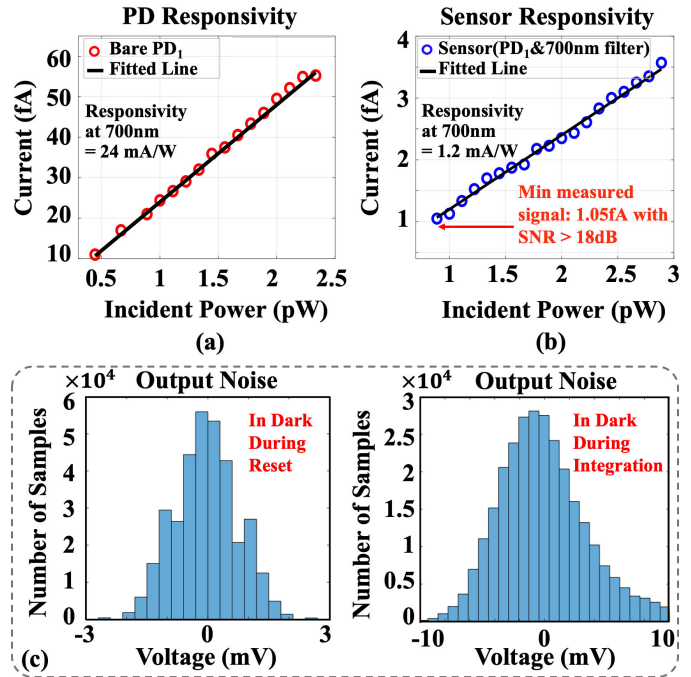

Fig. 20.   Measured responsivity of (a) bare PD1 at 700 nm, (b) sensor at 700 nm, and (c) measured noise histogram in the dark during the reset and integration phases.

the minimum measured signal of the sensor, including the 700-nm filter and PD1, is 1.05 fA, and the responsivity of the combination is 1.2 mA/W. The sensor noise is measured during the reset and integration phases under dark ambient conditions. The higher noise during the integration phase compared with the reset phase arises from the shot noise of the reset switch of the C-TIA. The leakage of this switch's OFF-current can be minimized by adding more transistors in series to reduce the effective off-voltage across each transistor. The measured noise statistics during the reset and integration phases are plotted in Fig. 20(c). When computing the total integrated noise from the PSD, we obtain 0.78 mV_{rms} during reset and 3.77 mV_{rms} during integration, resulting in an effective measured output noise of 3.85 mV_{rms}.

Fig. 21 shows the measured spectrum of the bare PDs and selected filters using dark PDs as a reference. As expected, PD2 has higher rejection at the lower wavelength range than PD1. Filters characterizations using PD1 show that

1-D filters have a primary peak at the 600-nm range and a second peak at around 700 nm while the 2-D filters have a single peak at the 700-nm range, confirming their polarization-insensitive response.

As discussed before, the sensor's ability to reject the undesirable EX signal is improved in the electrical domain thanks to its differential design, current compensating scheme,

This article has been accepted for inclusion in a future issue of this journal. Content is final as presented, with the exception of pagination.
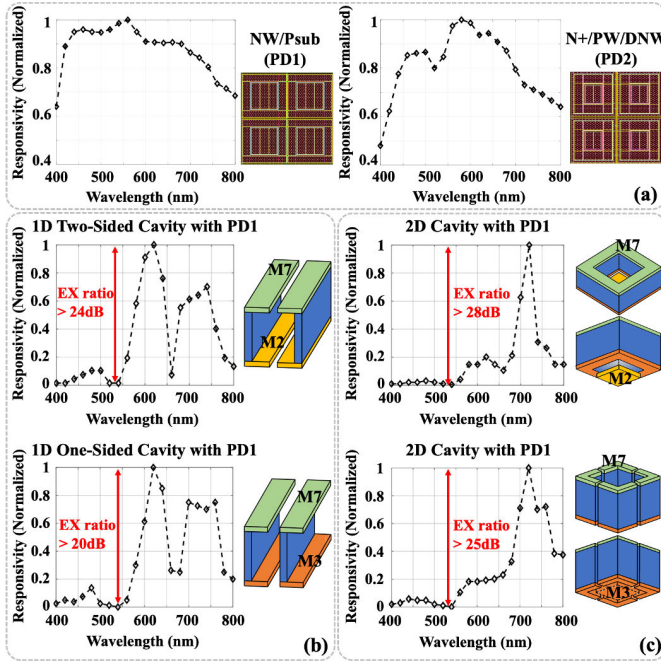
12

IEEE JOURNAL OF SOLID-STATE CIRCUITS

Fig. 21. Measured spectrum of (a) Bare PD1 and PD2, (b) one-dimensional cavities on top of PD1, and (c) two-dimensional cavities on top of PD1.
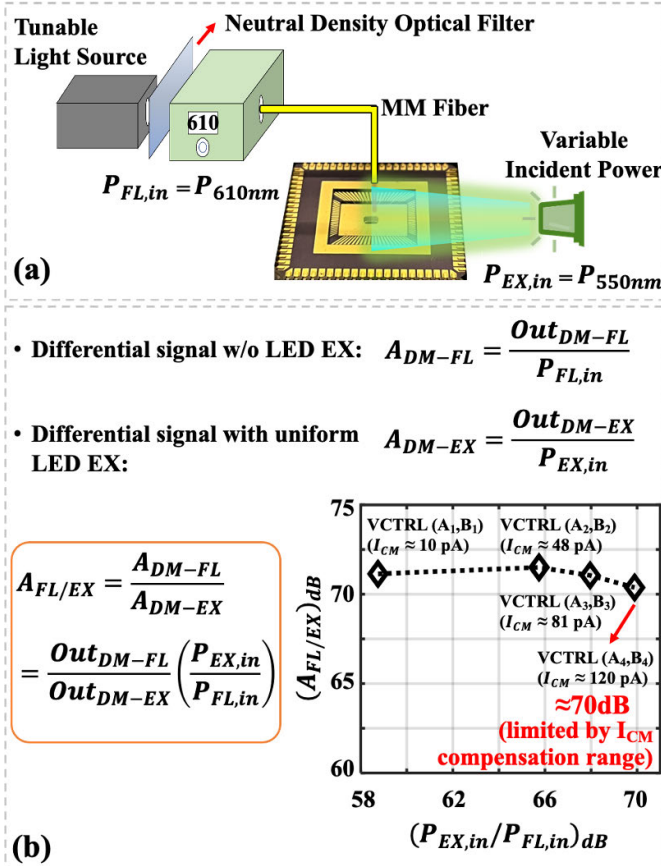

Fig. 22. Measuring the total rejection ratio of the sensor. (a) Setup includes a uniform LED as CM excitation and a tunable light source as a differential signal. (b) Measured the total rejection ratio of the sensor for various levels of LED incident power.
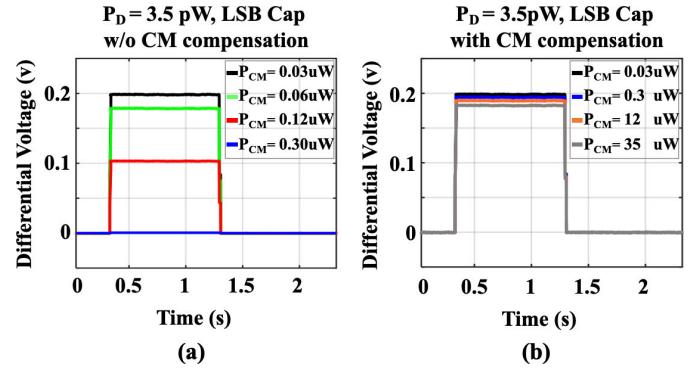

Fig. 23. Measured response of the sensor with LSB cap in use for various CM input power. (a) Without CM compensation. (b) With CM compensation.
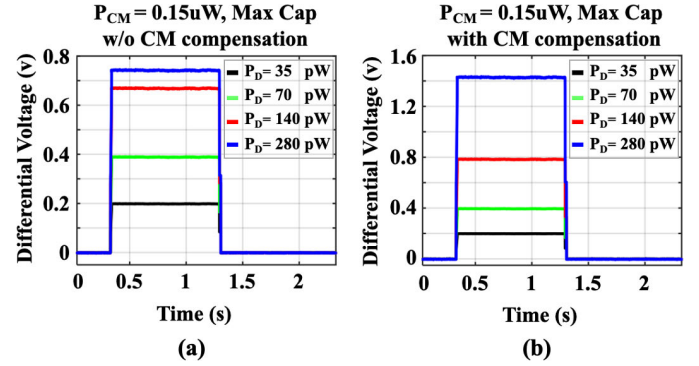

Fig. 24. Measured response of the sensor with the lowest gain settings for various differential input power. (a) Without CM compensation. (b) With CM compensation.
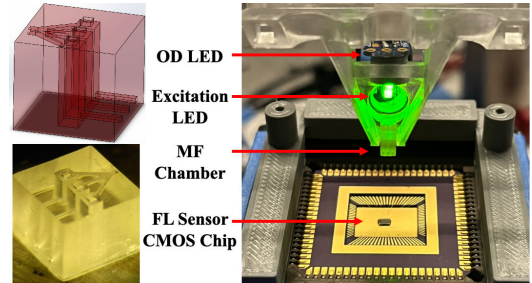

Fig. 25. Design and fabrication of the MF chamber and the fixture for biological experiments.

and configurable C-TIA that extends its dynamic range. Fig. 22 shows the measurement setup and result of the combined (including both optical and electrical) rejection ratio of the sensor. First, the desired signal with the fixed power $P_{\text{FL,in}}$ is applied to the sensor. In the absence of the excitation source, this differential light generates the desired differential output voltage, $\text{Out}_{\text{DM}-\text{FL}}$. Next, the excitation light, $P_{\text{EX,in}}$, is introduced such that it uniformly covers the whole surface of the sensor, resulting in an undesired differential component at the output, $\text{Out}_{\text{DM}-\text{EX}}$. As shown in Fig. 22, the total rejection of the excitation light is $A_{\text{FL/EX}}$ which is measured for various excitation power intensities. At each power level of $P_{\text{EX,in}}$, the VCCS block is tuned to provide the optimum CM compensation current, minimizing the circuit's response to the excitation light. This preserves the high rejection ratio for the practical range of $P_{\text{EX,in}}$. At very large values of the incident LED power, which in practice is avoided due to possible FP photobleaching, VCCS is close to the end of its range resulting in deterioration of the rejection ratio. The circuit's dynamic range is measured and plotted in Figs. 23 and 24, showing the

This article has been accepted for inclusion in a future issue of this journal. Content is final as presented, with the exception of pagination.

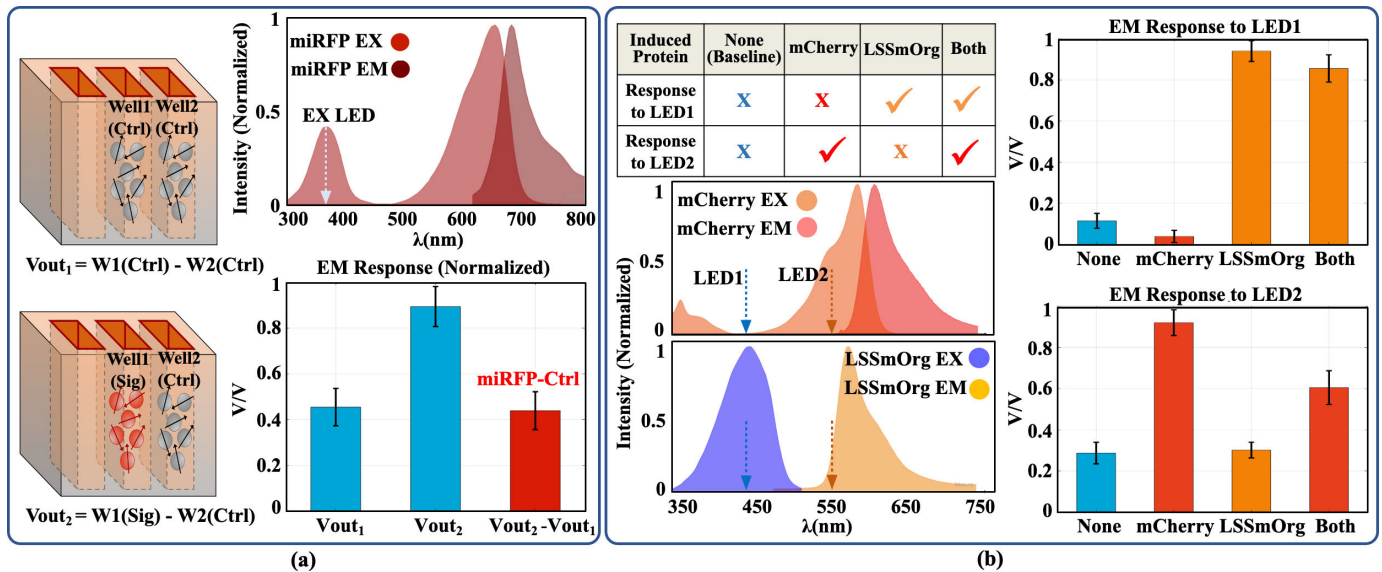AGHLMAND et al.: 65-nm CMOS FLUORESCENCE SENSOR FOR DYNAMIC MONITORING 13

Fig. 26. Static FL measurement results of (a) single protein named miRFP and (b) two proteins (mCherry and LSSmOrange) which are used for distinguishing two biochemicals in a culture.

TABLE I
CHIP PERFORMANCE SUMMARY

Technology	65nm CMOS
Differential Dark Currents (PD reverse bias=1.6V)	PD1 = 5.7fA PD2 = 7.8fA
Bare PD1 Responsivity	24mA/W
PD1 and 700nm Filter Sensitivity	1.2mA/W
Extinction Ratio (for an offset of 60nm between EX/EM)	Optically ≈ 30dB (Using PD2) Total ≈ 70dB (Optically and Electrically)
Dynamic Range	Differential: Up to 280pW Common-Mode: Up to 40uW
Excitation Source	Low - Cost LED

effect of the VCCS block and the variable capacitor bank in the C-TIA in extending the range of input signals (both differential mode and CM). Table I summarizes the key parameters of the FL sensor including the measured differential dark currents of the PDs, the total rejection ratio, and the dynamic range of the sensor.

The setup for biological measurements is shown in Fig. 25. A triple-well microfluidic chamber that has a 250-μm channel size and 5/10-μL volume for each well is designed and fabricated with bio-compatible resin. A fixture to place the LEDs for OD and FL measurements and the MF chamber is also fabricated. The first experiment is to detect a single FP with low brightness in the 700-nm range. A constitutive recombinant FP named miRFP [63] with two excitation peaks at 388 nm/674 nm and an emission peak at 700 nm is encoded in living *E. coli* bacterial cells for this experiment. To account for the non-uniform optical properties of the adjacent wells, caused by the residual resin and manual cleaning process, we calibrated the setup using Ctrl culture which is the blank bacterial cells (w/o FP proteins) to establish the baseline. As shown in Fig. 26(a), V_{out1} is the difference in the emission

signal of the two control wells (W1 and W2). The center well (W1) is then replaced by the culture containing miRFP, and the emission is recorded as V_{out2}. Based on the definition shown in Fig. 26(a), the red bar shows the FL response of the miRFP.

The next experiment is designed to confirm the ability of the sensor to detect two biochemical signals reported by two FPs. The possible crosstalk error can be minimized by selecting two proteins with distinct enough excitation bands and using narrowband LEDs. For this experiment, two plasmids encoding mCherry [64] and LSSmOrange [65] FPs, under inducible promoters, are transformed into living *E. coli* cells. We measured the bacterial culture with four different induction profiles using chemical inducers; none, one, or both proteins were expressed, as shown in Fig. 26(b). By exciting cultures using LED1 and LED2 and observing distinct columns, the expression of a protein in the mixture is deduced. The measured results show that LSSmOrange protein responds to LED1 and mCherry protein to LED2. In addition, we observe that the signal of the non-responsive protein at each plot is around the baseline, and the response of the culture containing both biochemicals is around the signal of the responsive protein.

Observing gene expression dynamics in living cells requires measuring both cell growth and FL signal dynamics. The cell growth curve is achieved by recording the OD over time, showing the status of cells during their life cycle spanning from the lag phase to death in the decline phase. The most important part of the curve that shows the healthy growth of cells is the exponential phase. To minimize the delay caused by protein folding and maturation, we opted for super-folder YFP (sfYFP [66]), which has a rapid folding rate. Despite the emission peak of sfYFP not entirely being in the filter passband range, the strong brightness of this protein aids its detection in the non-peak wavelength of >580 nm. To achieve a robust signal, the collective response of multiple rows of the chip and the maximum gain settings are utilized. Furthermore, we employed a 500-nm LED as
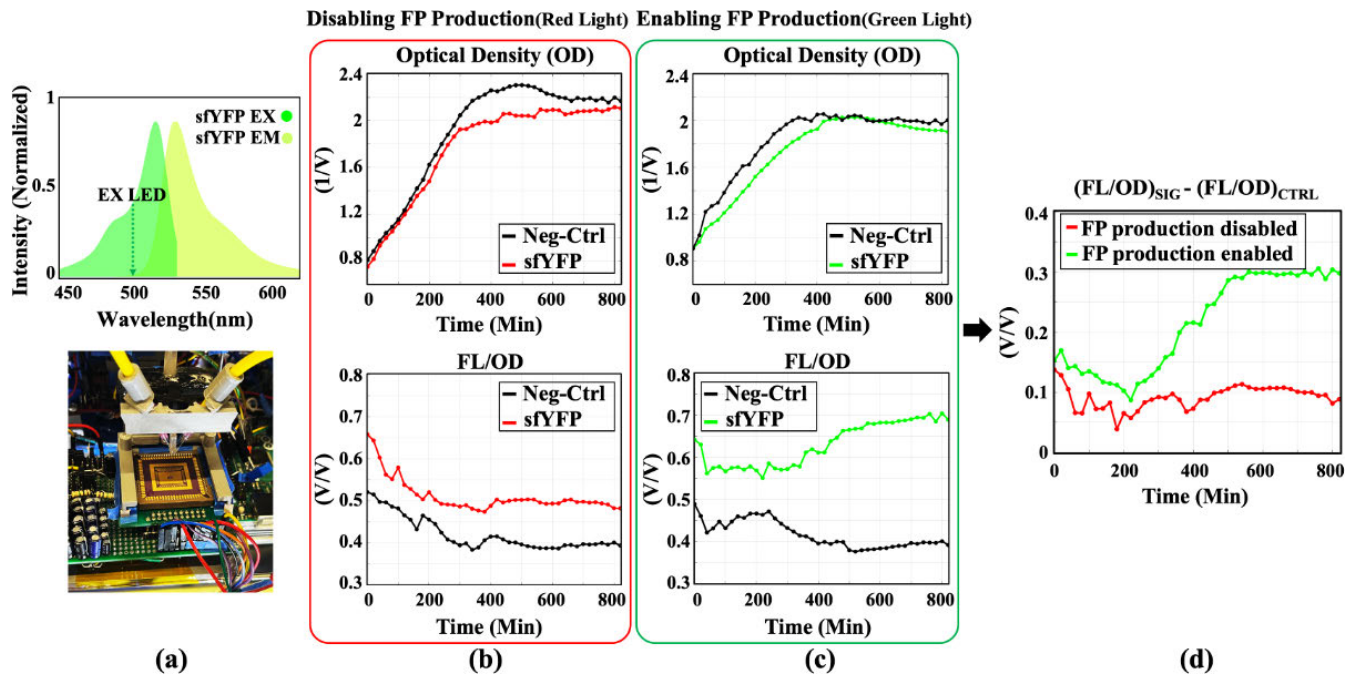
Fig. 27.   Dynamic FP measurements. (a) Spectrum of sfYFP and the measurement setup inside the incubator. (b) Measured results of OD and normalized FL expression when cells received a red light. (c) Measured results of OD and normalized FL expression when cells received a green light. (d) Plot shows modulation of the FP production using optogenetic control.

TABLE II
PERFORMANCE SUMMARY AND COMPARISON WITH THE STATE OF THE ART

	[5]	[19]	[67]	[68]	[62]	[69]	This Work
Technology	65nm CMOS	65nm CMOS	180nm CMOS	250nm CMOS	110nm CMOS	180nm CMOS	**65nm CMOS**
Detector Type	Fluorescence	Bioluminescence	Fluorescence	Fluorescence	Fluorescence	Fluorescence	**Fluorescence**
Optical Filter (CMOS)	Yes (High-pass)	No	No	No	No	No	**Yes (Band-pass)**
Reporter Type	Qdot800 tags	Luminescence Protein in bacterial cells	Qdot705 tags	DNA/RNA	DAPI and Qdot	N.R.	**Fluorescent Proteins in bacterial cells**
Measurement Type	Static	Static/Dynamic	Static	Static	Static	Benchtop	**Static / Dynamic (OD and FL signals)**
Excitation Source	405nm Laser	N.A.	Laser (Blue)	N.A.	472nm Laser	LED (530nm)	**SMD LED**
PD Active Area	91.4 x 123 μm^2	1.24 x 1.24 mm^2	55 x 55 μm^2	50 x 50 μm^2	11.2 x 5.6 μm^2	300 x 300 μm^2	**100 x 100 μm^2**
PD/Pixel Responsivity	22 mA/W (PD at 780nm)	N.R.	90.2 mA/W [#] (Pixel)	1e-9 fA/photons/cm^2/sec	N.R.	N.R.	**24 mA/W (PD at 700nm)**
Power	66mW *	16.3μW **	3.5mW ***	118mW	540mW	93μW	**1 Row:7.05mW**
Output Noise [##]	1.31mV_{rms}	N.R.	4.5mV_{rms}	N.R.	19.04mV_{rms}	N.R.	**3.846mV_{rms}**
Sensor Sensitivity	0.33fA (with T=10s)	59fA	N.R.	~10fA	137 ke^-/lux.sec	1300fA$_{rms}$	**1.05fA (with T=1s)**
Integration time	1-10s	25.8s	10-50ms	N.R.	N.R.	N.R.	**1s**
SNR	>20dB	N.R.	15.5dB	>20dB	N.R.	N.R.	**18.3dB**
Extinction Ratio	51dB	N.A.	N.R.	36dB	94%	N.R.	**70dB (combined optically and electrically)**

[#] Converted from reported pixel responsivity of 8.2V/pW.s, using Cfb=11fF and Tin=50ms.
* Reported for dual sensors
** Total capsule power for 2x2 array (including wireless radio)
*** Reported for 80 x 36 pixels array
[##] Under dark condition
N.A. – Not applicable
N.R. – Not reported

the excitation light, as this wavelength range is a strong dip in the measured filter spectrum and provides high optical filtering.

Modulating protein expression dynamics is critical in establishing a bidirectional communication link between cells and the CMOS chip. Optogenetic control encoded in the

engineered *E. coli* cells allows us to control protein expression using light sources. Fig. 27 shows that bacterial cells express sfYFP when exposed to a green light, and the FP expression is minimal when they are exposed to a red light. This accomplishment demonstrates the potential to create an integrative autonomous sensing and payload delivery bioelectronic system. For instance, in vivo targeted drug delivery can be achieved by sensing a biochemical indicating inflammation in the gut, and in response appropriate optical signaling can activate medication production and delivery to treat the detected inflammation. Hence, this cell-silicon system can create a promising platform for developing novel therapeutic approaches.

Table II shows the performance of the FL sensor in comparison with prior art. By using on-chip cavity structures in the standard CMOS process, we designed bandpass optical filters to realize a monolithic FL sensor that can detect the FPs engineered in live bacterial cells. In addition, monitoring the cell growth and their FL expression dynamics demonstrates the potential for controlling and creating various cellular functions. Our work uses low-cost LEDs for excitation, making the system suitable for portable personal applications. The sensor sensitivity measured with the practical integration time of 1 s shows competitive performance compared to [5] and [19] with 10–25 times higher T_{int}. Compared with [68] which uses post-processing steps for optical filter implementation and [5] which achieves a 51-dB (optically) extinction ratio for on-chip high pass filters, in our work, the rejection level of $\approx$70 dB is resulted by combining the bandpass optical filtering of the cavity structures and PDs and use of efficient circuit design techniques.

VII. Conclusion

This article presents an integrated FL sensor in standard CMOS that can enable bidirectional communication between live bacterial cells and the chip. The sensor realizes all the required components of FL sensing, including optical filters, PDs, and processing circuits. Using available metal routing layers in the 65-nm CMOS process, cavity resonators are implemented to achieve the bandpass optical filters in the wavelength range compatible with the most common FPs. The sensor measures a minimum signal of 1.05 fA with SNR > 18 dB while using the short integration time of 1s.

Acknowledgment

References

[1] A. Manickam, A. Chevalier, M. McDermott, A. D. Ellington, and A. Hassibi, "A CMOS electrochemical impedance spectroscopy (EIS) biosensor array," *IEEE Trans. Biomed. Circuits Syst.*, vol. 4, no. 6, pp. 379–390, Dec. 2010.

[2] P. M. Levine, P. Gong, R. Levicky, and K. L. Shepard, "Active CMOS sensor array for electrochemical biomolecular detection," *IEEE J. Solid-State Circuits*, vol. 43, no. 8, pp. 1859–1871, Aug. 2008.

[3] D. A. Hall, R. S. Gaster, K. A. A. Makinwa, S. X. Wang, and B. Murmann, "A 256 pixel magnetoresistive biosensor microarray in 0.18 μm CMOS," *IEEE J. Solid-State Circuits*, vol. 48, no. 5, pp. 1290–1301, May 2013.

[4] H. Wang, Y. Chen, A. Hassibi, A. Scherer, and A. Hajimiri, "A frequency-shift CMOS magnetic biosensor array with single-bead sensitivity and no external magnet," in *IEEE Int. Solid-State Circuits Conf. (ISSCC) Dig. Tech. Papers*, Feb. 2009, pp. 438–439.

[5] L. Hong, H. Li, H. Yang, and K. Sengupta, "Fully integrated fluorescence biosensors on-chip employing multi-functional nanoplasmonic optical structures in CMOS," *IEEE J. Solid-State Circuits*, vol. 52, no. 9, pp. 2388–2406, Sep. 2017.

[6] K. N. Daeffler et al., "Engineering bacterial thiosulfate and tetrathionate sensors for detecting gut inflammation," *Mol. Syst. Biol.*, vol. 13, no. 4, p. 923, Apr. 2017.

[7] S. Sharma et al., "3D surgical alignment with 100 μm resolution using magnetic-field gradient-based localization," in *IEEE Int. Solid-State Circuits Conf. (ISSCC) Dig. Tech. Papers*, Feb. 2020, pp. 318–320.

[8] D. T. Riglar et al., "Engineered bacteria can function in the mammalian gut long-term as live diagnostics of inflammation," *Nature Biotechnol.*, vol. 35, no. 7, pp. 653–658, Jul. 2017.

[9] M. Zourob, S. Elwary, and A. P. F. Turner, *Principles of Bacterial Detection: Biosensors, Recognition Receptors, and Microsystems*. New York, NY, USA: Springer, 2008.

[10] S. Leth et al., "Engineered bacteria based biosensors for monitoring bioavailable heavy metals," *Electroanalysis*, vol. 14, no. 1, pp. 35–42, Jan. 2002.

[11] S. Sharma et al., "Wireless 3D surgical navigation and tracking system with 100 μm accuracy using magnetic-field gradient-based localization," *IEEE Trans. Med. Imag.*, vol. 40, no. 8, pp. 2066–2079, Aug. 2021.

[12] C. P. Zschiedrich, V. Keidel, and H. Szurmant, "Molecular mechanisms of two-component signal transduction," *J. Mol. Biol.*, vol. 428, no. 19, pp. 3752–3775, Sep. 2016.

[13] A. Ivask, M. Virta, and A. Kahru, "Construction and use of specific luminescent recombinant bacterial sensors for the assessment of bioavailable fraction of cadmium, zinc, mercury and chromium in the soil," *Soil Biol. Biochemistry*, vol. 34, no. 10, pp. 1439–1447, Oct. 2002.

[14] P. Banerjee, S. Kintzios, and B. Prabhakarpandian, "Biotoxin detection using cell-based sensors," *Toxins*, vol. 5, no. 12, pp. 2366–2383, Nov. 2013.

[15] L. R. Joseph, *Principles of Fluorescence Spectroscopy*. New York, NY, USA: Springer, 2013.

[16] *Fluo Sens Integrated | DIALUNOX—Fluorescence Measurement*. DIALUNOX, Stockach, Germany, 2023. [Online]. Available: https://www.fluorescence-measurement.com

[17] L. Hong, H. Li, H. Yang, and K. Sengupta, "Integrated angle-insensitive nanoplasmonic filters for ultraminiaturized fluorescence microarray in a 65 nm digital CMOS process," *ACS Photon.*, vol. 5, no. 11, pp. 4312–4322, Sep. 2018.

[18] E. A. Rodriguez et al., "The growing and glowing toolbox of fluorescent and photoactive proteins," *Trends Biochem. Sci.*, vol. 42, no. 2, pp. 111–129, Feb. 2017.

[19] Q. Liu et al., "A threshold-based bioluminescence detector with a CMOS-integrated photodiode array in 65 nm for a multi-diagnostic ingestible capsule," *IEEE J. Solid-State Circuits*, vol. 58, no. 3, pp. 838–851, Mar. 2023.

[20] G. Patterson, R. N. Day, and D. Piston, "Fluorescent protein spectra," *J. Cell Sci.*, vol. 114, no. 5, pp. 837–838, Jan. 2001.

[21] M. T.-Q. Duong, Y. Qin, S.-H. You, and J.-J. Min, "Bacteria-cancer interactions: Bacteria-based cancer therapy," *Experim. Mol. Med.*, vol. 51, no. 12, pp. 1–15, Dec. 2019.

[22] S. Sharma, H. Melton, L. Edmonds, O. Addington, M. Shapiro, and A. Emami, "A monolithic 3D magnetic sensor in 65 nm CMOS with <10 μT$_{\text{rms}}$ noise and 14.8 μW power," in *Proc. IEEE Custom Integr. Circuits Conf. (CICC)*, Apr. 2023, pp. 1–2.

[23] K. Ghoreschi et al., "Interleukin-4 therapy of psoriasis induces Th2 responses and improves human autoimmune disease," *Nature Med.*, vol. 9, no. 1, pp. 40–46, Jan. 2003.

[24] S. Sharma et al., "Location-aware ingestible microdevices for wireless monitoring of gastrointestinal dynamics," *Nature Electron.*, vol. 6, no. 3, pp. 242–256, Feb. 2023.

This article has been accepted for inclusion in a future issue of this journal. Content is final as presented, with the exception of pagination.

16   IEEE JOURNAL OF SOLID-STATE CIRCUITS

[25] J. Ru, Y. Huo, and Y. Yang, "Microbial degradation and valorization of plastic wastes," *Frontiers Microbiol.*, vol. 11, p. 442, Apr. 2020.

[26] X. Xu et al., "Petroleum hydrocarbon-degrading bacteria for the remediation of oil pollution under aerobic conditions: A perspective analysis," *Frontiers Microbiol.*, vol. 9, Dec. 2018.

[27] D. Del Vecchio and R. M. Murray, *Biomolecular Feedback Systems*. Princeton, NJ, USA: Princeton Scholarship Online, 2017.

[28] N. T. Ong and J. J. Tabor, "A miniaturized *Escherichia coli* green light sensor with high dynamic range," *ChemBioChem*, vol. 19, no. 12, pp. 1255–1258, Jun. 2018.

[29] F. Aghimand, C. Hu, S. Sharma, K. K. Pochana, R. M. Murray, and A. Emami, "A 65 nm CMOS living-cell dynamic fluorescence sensor with 1.05 fA sensitivity at 600/700 nm wavelengths," in *IEEE Int. Solid-State Circuits Conf. (ISSCC) Dig. Tech. Papers*, Feb. 2023, pp. 311–313.

[30] (Jan. 29, 2023). *Fluorescence*. [Online]. Available: https://chem.libretexts.org/@go/page/1766

[31] L. Song, E. J. Hennink, I. T. Young, and H. J. Tanke, "Photobleaching kinetics of fluorescein in quantitative fluorescence microscopy," *Biophysical J.*, vol. 68, no. 6, pp. 2588–2600, Jun. 1995.

[32] F. Widdel, "Theory and measurement of bacterial growth," *Grundpraktikum Mikrobiologie*, vol. 4, pp. 1–11, May 2007.

[33] Q. Chen, X. Hu, L. Wen, Y. Yu, and D. R. S. Cumming, "Nanophotonic image sensors," *Small*, vol. 12, no. 36, pp. 4922–4935, May 2016.

[34] Q. Chen et al., "A CMOS image sensor integrated with plasmonic colour filters," *Plasmonics*, vol. 7, pp. 695–699, Dec. 2012.

[35] Q. Wang, Z. Zhu, H. Gu, and Q. Tan, "Angle-tolerant hybrid plasmonic blue filter with polarization-insensitivity and high transmission," *Opt. Commun.*, vol. 427, pp. 457–461, Nov. 2018.

[36] C. Yang et al., "Angle robust reflection/transmission plasmonic filters using ultrathin metal patch array," *Adv. Opt. Mater.*, vol. 4, no. 12, pp. 1981–1986, Sep. 2016.

[37] T. Wood et al., "All-dielectric color filters using SiGe-based Mie resonator arrays," *ACS Photon.*, vol. 4, no. 4, pp. 873–883, Mar. 2017.

[38] F. Shen, Q. Kang, J. Wang, K. Guo, Q. Zhou, and Z. Guo, "Dielectric metasurface-based high-efficiency mid-infrared optical filter," *Nanomaterials*, vol. 8, no. 11, p. 938, Nov. 2018.

[39] S. A. Maier, *Plasmonics: Fundamentals and Applications*. Berlin, Germany: Springer, 2007.

[40] S. A. Maier and H. A. Atwater, "Plasmonics: Localization and guiding of electromagnetic energy in metal/dielectric structures," *J. Appl. Phys.*, vol. 98, Jul. 2005, Art. no. 011101.

[41] F. Gildas and Y. Dan, "Review of nanostructure color filters," *J. Nanophotonics*, vol. 13, no. 2, 2019, Art. no. 020901.

[42] S. A. Maier, "Plasmonics: The promise of highly integrated optical devices," *IEEE J. Sel. Topics Quantum Electron.*, vol. 12, no. 6, pp. 1671–1677, Nov. 2006.

[43] J. Jiang et al., "Plasmonic nano-arrays for ultrasensitive bio-sensing," *Nanophotonics*, vol. 7, no. 9, pp. 1517–1531, Aug. 2018.

[44] A. Kausar, A. Reza, T. Latef, M. Ullah, and M. Karim, "Optical nano antennas: State of the art, scope and challenges as a biosensor along with human exposure to nano-toxicology," *Sensors*, vol. 15, no. 4, pp. 8787–8831, Apr. 2015.

[45] M. Février, P. Gogol, J. M. Lourtioz, and B. Dagens, "Metallic nanoparticle chains on dielectric waveguides: Coupled and uncoupled situations compared," *Opt. Exp.*, vol. 21, no. 21, pp. 24504–24513, Oct. 2013.

[46] Y. H. Jang, Y. J. Jang, S. Kim, L. N. Quan, K. Chung, and D. H. Kim, "Plasmonic solar cells: From rational design to mechanism overview," *Chem. Rev.*, vol. 116, no. 24, pp. 14982–15034, Dec. 2016.

[47] D. Fleischman, L. A. Sweatlock, H. Murakami, and H. Atwater, "Hyper-selective plasmonic color filters," *Opt. Exp.*, vol. 25, no. 22, pp. 27386–27395, Oct. 2017.

[48] Y. Xu, J. Yue, M. Wang, X. Sun, and D. Zhang, "Tunable narrow-band filter based on long-range surface plasmon polariton waveguide Bragg grating," *Photonics*, vol. 9, no. 5, p. 344, May 2022.

[49] H. Liu and Z. Sun, "Narrow-band, low-sideband plasmonic filter of asymmetric bi-layer metallic nanoslit arrays," *Opt. Exp.*, vol. 29, no. 9, pp. 13590–13599, Apr. 2021.

[50] W. L. Barnes, A. Dereux, and T. W. Ebbesen, "Surface plasmon subwavelength optics," *Nature*, vol. 424, no. 6950, pp. 824–830, Aug. 2003.

[51] S. Pi et al., "Dielectric-grating-coupled surface plasmon resonance from the back side of the metal film for ultrasensitive sensing," *IEEE Photon. J.*, vol. 8, no. 1, pp. 1–7, Feb. 2016.

[52] E. Popov, S. Enoch, G. Tayeb, M. Neviere, B. Gralak, and N. Bonod, "Enhanced transmission due to non-plasmon resonances in one and two-D gratings," *Appl. Opt.*, vol. 43, no. 5, pp. 999–1008, 2004.

[53] M. Neviere, E. Popov, R. Reinisch, and G. Vitrant, *Electromagnetic Resonances in Nonlinear Optics*. Boca Raton, FL, USA: CRC Press, 2000.

[54] W. S. C. Chang, *Principles of Optics for Engineers: Diffraction and Modal Analysis*. Cambridge, U.K.: Cambridge Univ. Press, 2015.

[55] I. Avrutsky, E. M. Smith, S. Vangala, R. Gibson, J. R. Hendrickson, and J. W. Cleary, "Angle-and polarization-independent mid-infrared narrowband optical filters using dense arrays of resonant cavities," *Opt. Exp.*, vol. 27, no. 26, pp. 37481–37493, Dec. 2019.

[56] J. Zhou and L. J. Guo, "Achieving angle-insensitive spectrum filter with the slit nanoresonator array structure," *J. Nanophotonics*, vol. 9, no. 1, Dec. 2014, Art. no. 093795.

[57] D. Van Labeke, D. Gérard, B. Guizal, F. I. Baida, and L. Li, "An angle-independent frequency selective surface in the optical range," *Opt. Exp.*, vol. 14, no. 25, pp. 11945–11951, Sep. 2006.

[58] S. Mehta, U. Jeong, J. Liu, and B. Guo, "Critical doping requirements for ≤65 nm device manufacturing," *Mater. Sci. Eng., B*, vol. 114, pp. 72–76, Dec. 2004.

[59] Y.-M. Sheu et al., "Modeling mechanical stress effect on dopant diffusion in scaled MOSFETs," *IEEE Trans. Electron Devices*, vol. 52, no. 1, pp. 30–38, Jan. 2005.

[60] Y. Li and S.-M. Yu, "A coupled-simulation-and-optimization approach to nanodevice fabrication with minimization of electrical characteristics fluctuation," *IEEE Trans. Semicond. Manuf.*, vol. 20, no. 4, pp. 432–438, Nov. 2007.

[61] K. Inoue et al., "Three-dimensional dopant characterization of actual metal–oxide–semiconductor devices of 65 nm node by atom probe tomography," *Appl. Phys. Exp.*, vol. 6, no. 4, Apr. 2013, Art. no. 046502.

[62] M.-W. Seo et al., "A 10 ps time-resolution CMOS image sensor with two-tap true-CDS lock-in pixels for fluorescence lifetime imaging," *IEEE J. Solid-State Circuits*, vol. 51, no. 1, pp. 141–154, Jan. 2016.

[63] K. D. Piatkevich et al., "A robotic multidimensional directed evolution approach applied to fluorescent voltage reporters," *Nature Chem. Biol.*, vol. 14, no. 4, pp. 352–360, Feb. 2018.

[64] N. C. Shaner, R. E. Campbell, P. A. Steinbach, B. N. Giepmans, A. E. Palmer, and R. Y. Tsien, "Improved monomeric red, orange and yellow fluorescent proteins derived from *Discosoma* sp. Red fluorescent protein," *Nat. Biotechnol.*, vol. 22, pp. 1567–1572, Nov. 2004.

[65] D. M. Shcherbakova, M. A. Hink, L. Joosen, T. W. J. Gadella, and V. V. Verkhusha, "An orange fluorescent protein with a large Stokes shift for single-excitation multicolor FCCS and FRET imaging," *J. Amer. Chem. Soc.*, vol. 134, no. 18, pp. 7913–7923, Apr. 2012.

[66] J.-D. Pédelacq, S. Cabantous, T. Tran, T. C. Terwilliger, and G. S. Waldo, "Engineering and characterization of a superfolder green fluorescent protein," *Nature Biotechnol.*, vol. 24, no. 1, pp. 79–88, Jan. 2006.

[67] E. P. Papageorgiou, B. E. Boser, and M. Anwar, "Chip-scale angle-selective imager for in vivo microscopic cancer detection," *IEEE Trans. Biomed. Circuits Syst.*, vol. 14, no. 1, pp. 91–103, Feb. 2020.

[68] A. Manickam et al., "A fully integrated CMOS fluorescence biochip for DNA and RNA testing," *IEEE J. Solid-State Circuits*, vol. 52, no. 11, pp. 2857–2870, Nov. 2017.

[69] M. N. Khiarak, S. Martel, Y. De Koninck, and B. Gosselin, "High-DR CMOS fluorescence biosensor with extended counting ADC and noise cancellation," *IEEE Trans. Circuits Syst. I, Reg. Papers*, vol. 66, no. 6, pp. 2077–2087, Jun. 2019.

[70] A. Emami and S. Sharma, "3D localization of miniaturized devices for precision medicine," *IEEE Solid-State Circuits Mag.*, vol. 15, no. 2, pp. 41–48, Spring 2023.

Fatemeh Aghlmand (Member, IEEE) received the B.S. degree in electrical engineering from the University of Tehran, Tehran, Iran, and the M.S. degree in microelectronics from the Sharif University of Technology, Tehran. She is currently pursuing the Ph.D. degree in electrical engineering with the MICS Laboratory, California Institute of Technology (Caltech), Pasadena, CA, USA.

After working as an Analog IC Designer at EPFL, Lausanne, Switzerland. Her research interests are analog/mixed-signal and optical circuits and systems for biomedical and environmental applications.

Chelsea Y. Hu received the B.S. degree in chemical engineering from UCLA, Los Angeles, CA, USA, in 2013, and the Ph.D. degree in chemical engineering from Cornell University, Ithaca, NY, USA, in 2018.

After graduate school, she worked as a Post-Doctoral Scholar at the California Institute of Technology (Caltech), Pasadena, CA, USA, from 2018 to 2022. She is currently an ACES Assistant Professor in chemical engineering at Texas A&M University, College Station, TX, USA. Her research focuses on system dynamics and feedback control in synthetic biology.

Saransh Sharma (Member, IEEE) received the B.Tech. degree in electronics and electrical communication engineering from the Indian Institute of Technology (IIT) Kharagpur, Kharagpur, India, in 2017, and the M.S. degree in electrical engineering from the California Institute of Technology (Caltech), Pasadena, CA, USA, in 2018, where he is currently pursuing the Ph.D. degree in analog and mixed-signal integrated circuits and system design, with special emphasis on low-power biomedical applications.

Prof. Sharma was a recipient of the Jakob van Zyl Predoctoral Research Award and the Charles Lee Powell Fellowship at Caltech, the Viterbi India Scholarship, and the Kishore Vaigyanik Protsahan Yojana (KVPY) Fellowship.

Krishna Pochana (Member, IEEE) is currently pursuing the B.S. degree in electrical engineering with the California Institute of Technology (Caltech), Pasadena, CA, USA.

As part of his research at the MICS Laboratory, Caltech, he is involved with the design of microfluidic devices and embedded systems for use with synthetic biological cultures. His research interests include biomedical devices, micro/nanorobotics, robotic controls, and micro/nanofabrication schemes.

Prof. Pochana was a recipient of the 2023 Goldwater Scholarship Award and was named a 2021 Captain Pradeep B. Suklikar Memorial SURF Fellow at Caltech.

Richard M. Murray (Fellow, IEEE) received the B.S. degree in electrical engineering from the California Institute of Technology (Caltech), Pasadena, CA, USA, in 1985, and the M.S. and Ph.D. degrees in electrical engineering and computer Sciences from the University of California, Berkeley, CA, USA, in 1988 and 1991, respectively.

He is currently the Thomas E. and Doris Everhart Professor of control and dynamical systems and bioengineering at Caltech. His research is in the application of feedback and control to networked systems, with applications in biology and autonomy. Current projects include the analysis and design of biomolecular feedback circuits, the synthesis of discrete decision-making protocols for reactive systems, and the design of highly resilient architectures for autonomous systems.

Azita Emami (Senior Member, IEEE) received the B.S. degree from the Sharif University of Technology, Tehran, Iran, in 1996, and the M.S. and Ph.D. degrees in electrical engineering from Stanford University, Stanford, CA, USA, in 1999 and 2004, respectively.

From 2004 to 2006, she was with the IBM T. J. Watson Research Center, Yorktown Heights, NY, USA. She joined the California Institute of Technology (Caltech), Pasadena, CA, USA, in 2007, where she is currently the Andrew and Peggy Cherng Professor of electrical engineering and medical engineering and the Director of the Center for Sensing to Intelligence. She also serves as the Executive Officer (Head) of Department of Electrical Engineering. Her current research interests include integrated circuits and systems, integrated photonics, wearable and implantable devices for neural recording, neural stimulation, sensing, and drug delivery.

Dr. Emami was an IEEE Solid-State Circuits Society (SSCS) Distinguished Lecturer from 2017 to 2018. From 2016 to 2021, she was an Associate Editor of the IEEE JOURNAL OF SOLID-STATE CIRCUITS (JSSC).